small methods
www.small-methods.com

Recent Advances on Pulsed Laser Deposition of Large-Scale Thin Films

Jing Yu, Wei Han, Abdulsalam Aji Suleiman, Siyu Han, Naihua Miao,* and Francis Chi-Chung Ling**

2D thin films, possessing atomically thin thickness, are emerging as promising candidates for next-generation electronic devices, due to their novel properties and high performance. In the early years, a wide variety of 2D materials are prepared using several methods (mechanical/liquid exfoliation, chemical vapor deposition, etc.). However, the limited size of 2D flakes hinders their fundamental research and device applications, and hence the effective large-scale preparation of 2D films is still challenging. Recently, pulsed laser deposition (PLD) has appeared to be an impactful method for wafer-scale growth of 2D films, owing to target-maintained stoichiometry, high growth rate, and efficiency. In this review, the recent advances on the PLD preparation of 2D films are summarized, including the growth mechanisms, strategies, and materials classification. First, efficacious strategies of PLD growth are highlighted. Then, the growth, characterization, and device applications of various 2D films are presented, such as graphene, h-BN, MoS_2, BP, oxide, perovskite, semi-metal, etc. Finally, the potential challenges and further research directions of PLD technique is envisioned.

1. Introduction

The atomic thickness, absence of dangling bonds, flexibility, and quantum confinement effects of 2D materials, including graphene, boron nitride (BN), and transition-metal dichalcogenides (TMDs), have established them as highly viable options for future electronic applications.[1–8] 2D materials are commonly produced through either bottom-up techniques such as chemical vapor deposition (CVD),[2,6,9,10] atomic layer deposition (ALD),[11] and molecular beam epitaxy (MBE),[12] pulsed laser deposition (PLD),[13–17] etc.) or top-down methods such as physical exfoliation,[18–20] solution exfoliation,[21] etc. The dimensions of samples generated through physical exfoliation and solution exfoliation are constrained, and their thickness is indeterminate.[22–25] The prerequisite for meeting the demands of forthcoming industrial applications is the utilization of dependable preparation techniques for the synthesis of extensive, superior-quality 2D crystal films.[26–28] CVD, ALD, MBE, and PLD have widely utilized techniques for the synthesis of comprehensive 2D films.[29–33] Nevertheless, the level of controllability and repeatability exhibited by CVD is relatively low.[34–36] The preparation of non-layered oxides by ALD necessitated the utilization of costly organic gas sources, rendering it an infrequently employed technique for the production of 2D film.[11] The cost of MBE is prohibitively high, and its feasibility for large-scale production of 2D films in the future is questionable.[12] As for PLD method, we could make large-scale thin film cheaply and at high speed.[15,23] The PLD method has the capability of producing large-scale thin films at a rapid pace and low cost. In contrast to alternative other bottom-up film

J. Yu, F. C.-C. Ling
Department of Physics
The University of Hong Kong
Hong Kong 999077, P. R. China
E-mail: ccling@hku.hk

J. Yu
Department of Physics and Astronomy
University of Manchester
Manchester M13 9PL, UK

W. Han
Hubei Yangtze Memory Laboratories
Wuhan 430205, P. R. China

W. Han
School of Microelectronics
Hubei University
Wuhan 430062, P. R. China

A. A. Suleiman
Institute of Materials Science and Nanotechnology
Bilkent University UNAM
Ankara 06800, Turkey
E-mail: abdulsalam@unam.bilkent.edu.tr

S. Han, N. Miao
School of Materials Science and Engineering
Beihang University
Beijing 100191, P. R. China
E-mail: nhmiao@buaa.edu.cn

The ORCID identification number(s) for the author(s) of this article can be found under https://doi.org/10.1002/smtd.202301282

DOI: 10.1002/smtd.202301282

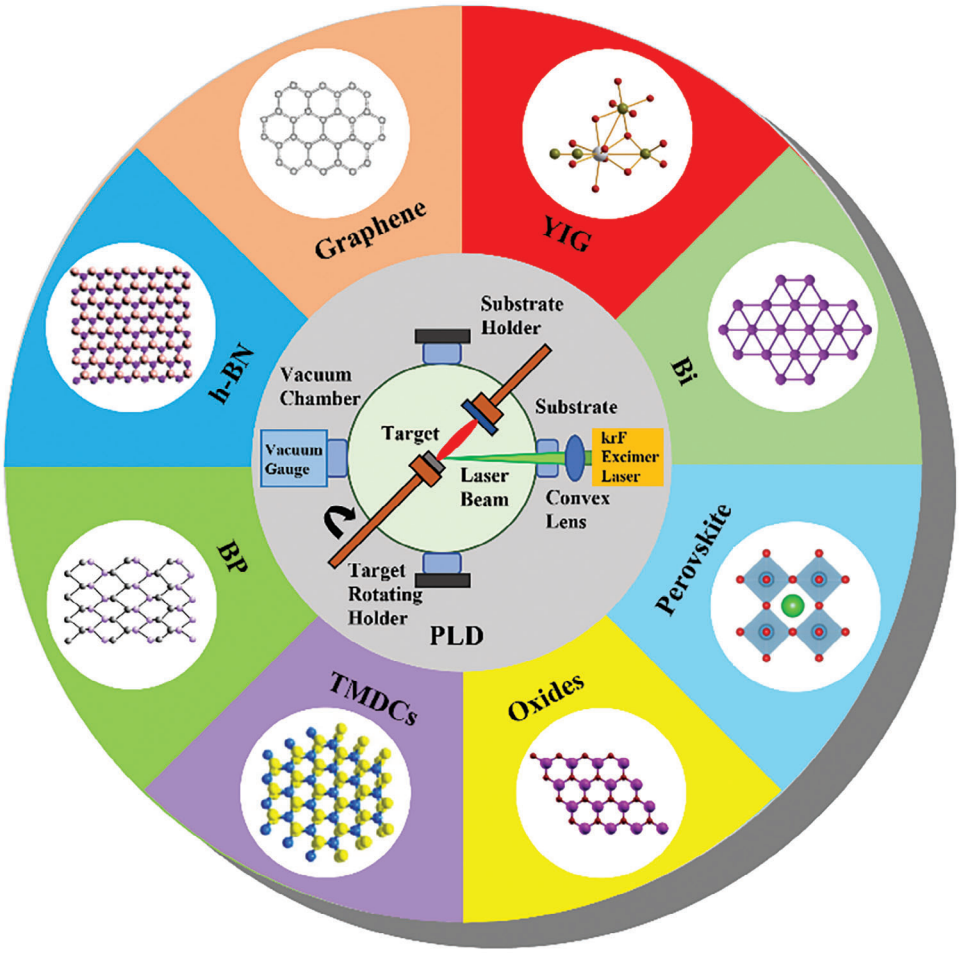

Figure 1. Schematic diagram of PLD method and various grown wafer-scale 2D films.

deposition techniques, PLD offers precise control over film composition and thickness, ensuring conformity with the stoichiometric ratio of the target composition.[17,23] This makes it a viable option for the growth of epitaxial films containing complex oxides.[16,23] The utilization of PLD technology is highly suitable for the production of intricate and manageable oxides. Moreover, PLD exhibits cost-effectiveness and demonstrates rapid growth in terms of speed.[23] Although PLD is an effective mean of preparing wafer-scale 2D materials, however, a complete and critical review including new methods and strategies is missing in the last 5 years. A comprehensive summary of recent applications and development of PLD techniques need to be introduced.

Herein, we have provided a comprehensive overview of the latest developments in the preparation of 2D films using PLD. The fundamental focus of this review is centered on elucidating the methodology for producing superior 2D thin films via PLD. This includes a discussion of the growth mechanisms, various strategies employed, and the classification of materials used. First, efficacious strategies for PLD growth are highlighted. Subsequently, an exposition is provided on the growth, characterization, and utilization of diverse 2D films, including graphene, h-BN, MoS_2, BP, oxides, perovskite, semi-metals, and others, in device applications. Finally, the challenges that must be addressed and the areas of further research emphasis on the PLD technique are presented.

2. Overview of PLD for 2D Films

The ultilization of PLD technology is prevalent in preparing various types of 2D materials, as illustrated in **Figure 1**. This section provides a comprehensive overview of the procedures involved in the preparation of epitaxial films using PLD systems. Specifically, the discourse delves into the equipment calibration, epitaxial film growth mechanism, identification of optimal growth conditions, and characterization techniques for these films.

2.1. Equipment Calibration

The process of PLD involves using a pulsed laser directed toward a target material, as depicted in **Figure 2**. When the laser energy density reaches a certain threshold, the material is vaporized or ablated by each laser pulse, resulting in the formation of a plasma plume (t = 0.1 μs). The material that has undergone ablation is expelled from the target in a plume that exhibits a significant degree of forward directionality (t = 2 μs). The expulsion of material

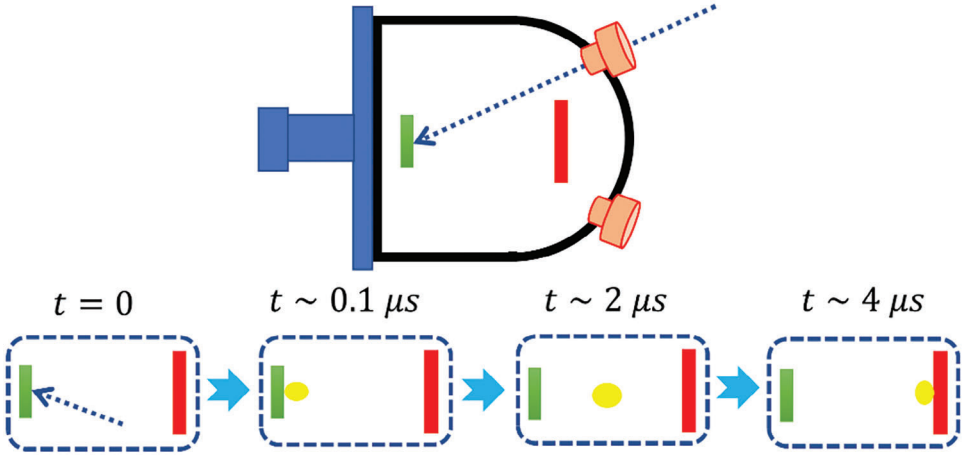

Figure 2. Process of PLD growth within a single pulse cycle.

from a surface, commonly known as the ablation plume, serves as the source of material flux that facilitates the growth of thin films (t = 2 μs).

The PLD technique has demonstrated remarkable efficacy in producing epitaxial films for multicomponent inorganic materials. The ablation parameters are selected to ensure the ablation plume is predominantly composed of low-mass species, such as atomic and diatomic particles. The customary approach involves the selection of a wavelength for an UV laser and a nanosecond pulse width that is highly absorbed by a limited portion of the material being targeted. The generation of plasma is attributed to the absorption of laser energy by the expelled material. Optimal conditions can be selected for the deposition of macromolecular organic materials, in which absorption occurs over a greater volume while minimizing laser absorption in the plume. This allows for a significant portion of the molecular substance to be ablated without fragmentation. The transfer of complete polymer chains has been exhibited in polymeric materials. The use of laser absorption in materials that are considered to be "softer" and could potentially cause damage to molecular functionality has been explored. To address this issue, composite ablation targets have been developed, which involve embedding the soft component in an optically absorbing matrix.

PLD exhibits three primary characteristics. At first, the synthesis process is executed in a pulsed mode, which enables the rapid growth of a minuscule quantity of a substance within a matter of microseconds. Furthermore, the expeditious and intense heating of the substrate in PLD facilitates the attainment of stoichiometric growth. The employment of the PLD method results in the generation of laser-ablated species that possess substantial kinetic energy, reaching up to a few keV. This feature enables the deposition of thin films that exhibit strong adhesion properties while being subjected to relatively low temperatures compared to alternative techniques. In the ultrahigh vacuum (UHV) chamber, targets composed of elementary, or alloy elements are subjected to a high-energy, focused pulsed laser beam at a 45° angle.

2.2. Epitaxial Film Growth Mechanism

After the particles at the end of the feather reach the substrate, they diffuse and migrate on the substrate, forming nuclei, growing, and re-evaporation. This process involves a series of thermodynamic and kinetic processes: the gas phase condenses into a solid phase, the free energy decreases, and the crystal nucleus exposes new surfaces and interfaces and raises the free energy, which together determines the growth process of the shape nucleus of the film. In general, under the premise that the particles reach the substrate with a certain amount of energy, the lattice constant and temperature of the substrate play a decisive role in the growth of the film's nucleus. If the lattice constant of the substrate differs significantly from the lattice constant of the target film, the interfacial energy of the crystal nucleus is large, and growth is more difficult. The right temperature can ensure that the particles have a sufficient diffusion distance, and the crystal nuclei are more likely to spread out in a wet state, which is conducive to its growth. Different growth conditions lead to three different film growth patterns, as shown in **Figure 3**, and the growth pattern of the film can be roughly determined by characterizing the surface morphology by atomic force microscopy.[37]

1) 3D island growth mode: The film grown in this form is rough, and the atomic force microscope morphology is like a forest. 2) 3D island growth and 2D layered growth mode (2D + 3D growth mode): The films that have grown in this mode mostly manifest as many bumps on the plane. 3) 2D layered growth (2D growth mode): Only this mode can grow out of the epitaxial film; the entire film is a single crystal, and the surface roughness is very small.

In general, to prepare an epitaxial film, it is necessary to control these three stages and thus the appropriate amount of material can be evaporated after a suitable distance, so that the substance with the appropriate energy and size reaches the substrate, and migrates in the proper substrate temperature, shapes the nucleus, and grows.

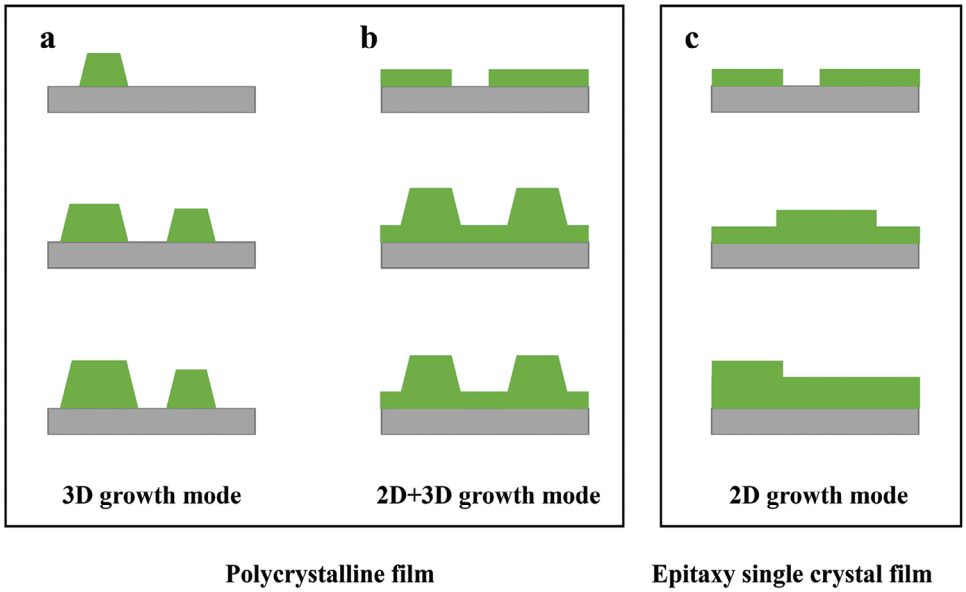

Figure 3. Film growth model of PLD process.

2.3. Identification of Optimal Growth Conditions

The procedures involved in the preparation of PLD films were comprehensively examined. The presence of a typical plume and the appropriate deposition temperature are prerequisites for the production of high-quality films, while the growth window has a constrained range. This section provides a comprehensive discussion on the growth of epitaxial films using PLD systems. Given the narrow growth window and the need for stringent control of each step. The production of high-quality films during the PLD process is dependent on several factors, including the manipulation of deposition time, temperature, gas pressure, gas composition, substrate, the distance between target and substrate, laser intensity, and the elemental composition of the target by the researchers. The duration of the deposition process may have an impact on the thickness of thin films. The quality of thin film crystals may be impacted by the duration of deposition. The utilization of O_2 gas during the production of thin film oxides is recommended as it enhances the quality of the film and reduces the occurrence of oxygen defects. Various substrates can be utilized for diverse applications or distinct material characteristics. Mica possesses a layered structure that presents the potential to obtain a monolayer film. Electric devices can be directly prepared by depositing thin films on SiO_2/Si or Si substrates. The utilization of sapphire substrate, owing to its *c*-orientation, has the potential to facilitate the attainment of high-quality films. Sapphire and glasses possess transparency, thereby enabling the evaluation of the optical characteristics of thin films.

2.4. Characterization Techniques

After obtaining the PLD grown film, how to characterize the material is also a very critical step. We use various modern technologies to characterize the PLD thin film materials. The nature and uniform surface of the film could be confirmed by various techniques, including XRD, TEM, Raman spectroscopy, AFM and so on. The film's appearance can be observed through photographs and optical micrographs. Material identification methods such as XRD, XPS, and Raman can help researchers to identify material composition. PL could help to obtain the optical band gap of the thin film material. AFM, SEM, and EDS mapping were used to obtain the surface morphology. At the same time, EDS mapping could help to get the information of elements composition. TEM can help to obtain the atomic arrangement of materials.

3. Graphene Grown Using PLD

The production of graphene film can be achieved through various methods, such as physical exfoliation, CVD, liquid phase methods, or epitaxial growth on silicon carbide (SiC). However, PLD stands out due to its distinctive benefits in comparison to the aforementioned techniques. The presence or absence of a metallic catalyst is a crucial factor in the advancement of PLD graphene growth. About a decade ago, PLD graphene growth without a catalytic nickel layer has been reported by Qian et al. and Kumar et al.[38,39] On the contrary, numerous recent scholarly studies have documented the production of graphene through the employment of the PLD technique with Ni catalysts, owing to the carbon segregation that occurs at elevated temperatures. Due to the elevated solubility of carbon in Ni, the carbon atoms diffuse through the Ni catalyst before precipitating on the catalyst's surface during the cooling process. A potential method for using Ni catalyst entails the initial deposition of Ni catalyst onto the intended substrate, then the subsequent deposition of a thin film of C. In 2019, Bleu et al. published a comparative research of graphene films grown on Si (100) or fused Silica (SiO_2) by PLD and rapid thermal annealing with Ni catalyst (**Figure** 4a).[40] Multilayered graphene grown on Si (100), and different nickel silicide phases formed under it. Mainly bilayered and trilayered graphene films grown on SiO_2, with no traces of nickel silicide. The results help to understand how different combinations of substrate and

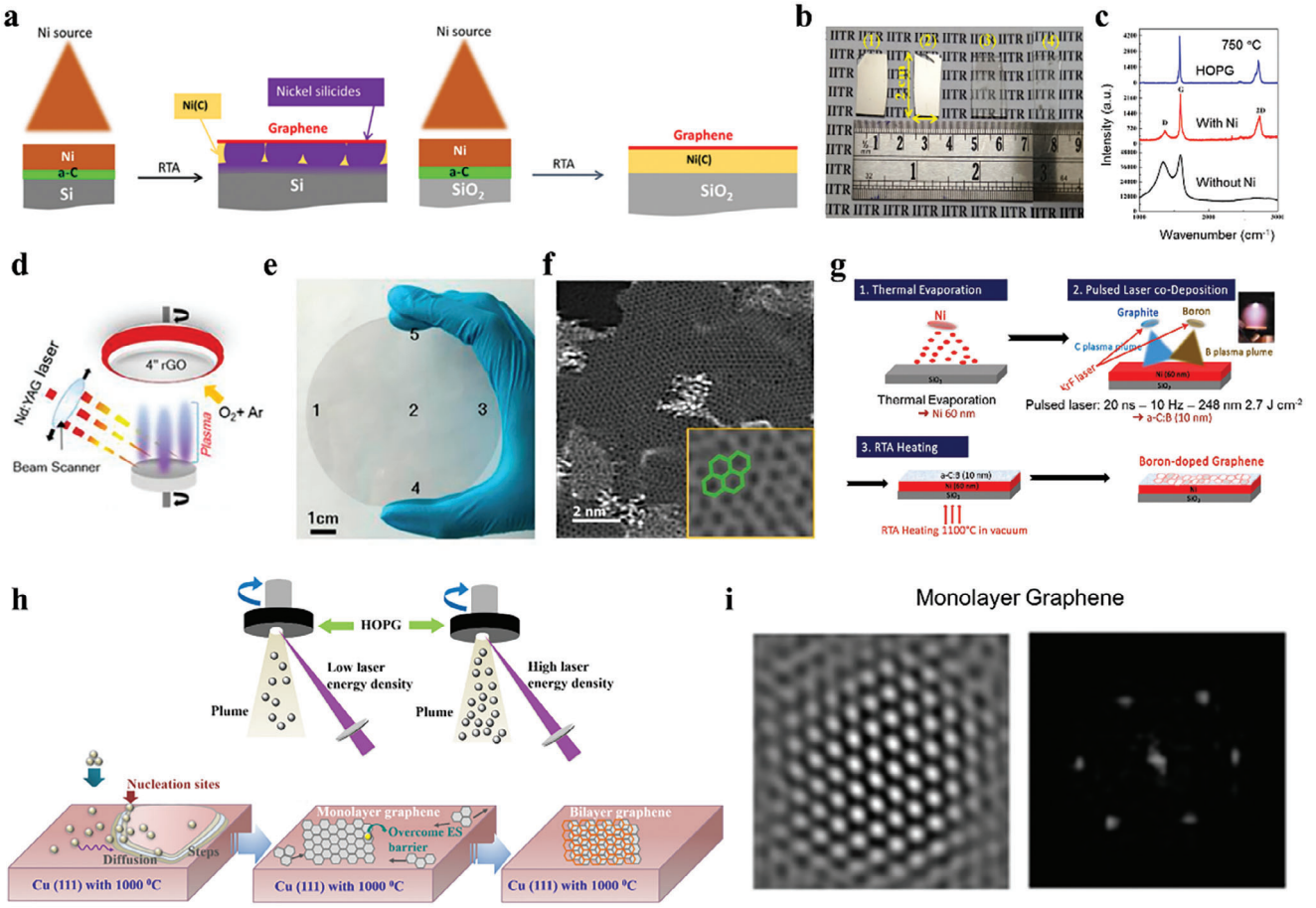

Figure 4. a) Growth route of graphene films obtained by PLD. b) Photos of the as-synthesized graphene samples on Ni-coated glass and glass. c) Raman spectra of HOPG and graphene grown on glass substrates with and without Ni catalytic layer. d) Schematic of PLD setup for growth of a 4-inch rGO film in a beam scanning mode. e) Photo of an ultrasmooth large-area rGO-like film on a 4-inch fused silica wafer. f) STEM image of PLD-grown rGO-like film consisting of a regular hexagonal carbon ring along with distorted hexagons due to functionalization and reduction. Inset: An enlarged STEM image showing predominantly hexagonal graphitic rings. g) Schematic illustration of large-scale N-doped graphene grown by PLD. h) Schematic diagram of graphene film growth by PLD. i) FFT and IFFT patterns of monolayer graphene sample. a) Reproduced with permission from ref. [40]. Copyright 2019, WILEY. All rights reserved. b,c) Reproduced with permission from ref. [45]. Copyright 2019, Elsevier. All rights reserved. d–f) Reproduced with permission from ref. [48]. Copyright 2020, American Chemical Society. All rights reserved. g) Reproduced with permission from ref. [49]. Copyright 2020, Elsevier. All rights reserved. h,i) Reproduced with permission from ref. [51]. Copyright 2019, Elsevier. All rights reserved.

thermal processing parameters impact the synthesis of graphene from solid carbon source with nickel catalyst. This would help to control defects and thickness of graphene layers and so on, which would also have a significant possibility for the development of graphene-based products.

It was determined that defect densities at 900 and 1000 °C are comparable to those generated by CVD, however defect densities at 800 °C are too low for graphene production because they result in a greater defect density.[41,42] In 2019, Bleu et al. successfully achieved the synthesis of bilayer graphene on SiO_2 through the employment of PLD technique, with the aid of Ni catalytic material. Initially, they conducted the synthesis of a-C: N films through PLD. Subsequently, they deposited Ni catalytic films onto the a-C: N film. Finally, they grew N-doped graphene through thermal heating, utilizing CN_x feedstock that was elaborated by PLD.[43] The study showcases the production of N-doped graphene with a doping concentration of ≈4%. Furthermore, a model was implemented to demonstrate the diffusion and segregation of carbon within the nickel film, thereby enabling a quantitative description of the growth of graphene. The study revealed that the expansion of graphene domains occurred at relatively low temperatures ranging from 200 to 300 °C. The accelerated transport of carbon was facilitated by the high density of defects and fine microstructure present in the nickel catalyst film, surpassing the rate of conventional bulk diffusion. At 500 °C, the carbon underwent bulk diffusion, which can be attributed to the recovery of the nickel grain microstructure. In contrast to the growth of graphene on a metal-catalyst-free substrate, using a nickel catalyst film with a refined microstructure and a high concentration of defects expedited carbon transportation, surpassing that of typical bulk diffusion. Utilizing the diffusion/segregation model presents a promising approach for enhancing the regulation of high-quality graphene growth. A previous study conducted by Hemani et al. documented the utilization of Ni catalysis in the growth of graphene through PLD.[44] They were able to produce interfacial bilayer graphene by employing a solid carbon source

in their PLD approach. Bilayer graphene was observed not only on the surface of nickel but also at the interface of nickel and SiO_2.[44]

The efficacy of Ni as a top layer on glass for forming graphene domains is recently demonstrated by Kumar et al.[45] The growth of few-layer graphene on a glass substrate was successfully achieved through the utilization of Ni film, as shown in Figure 4b. They also examined the impact of a Ni catalytic surface on the growth and structural integrity of graphene films that were synthesized on glass substrates through PLD. The utilization of this particular growth technique yields a noteworthy enhancement in the caliber of graphene films cultivated on glass substrates. This is substantiated by a decrease in defects and an augmentation in the crystalline nature of graphene films that incorporate Ni. The Raman spectra, as depicted in Figure 4c, provide conclusive evidence that Ni augmented the growth of graphene, and that the crystallinity of the graphene film was improved. Moreover, a decrease in the FWHM of the G-band and a rise in the intensity of the 2D-band are unequivocal markers of heightened graphitic clusters. Compared to the Wang et al. study, which showed the PLD of 2-, 3-, and few-layer graphene on catalytic nickel thin film at 650 °C.[46] Where they demonstrated that the formation of graphene layers' thickness is contingent upon the film thickness ratios of C to Ni, which can be accurately manipulated by altering the duration of laser ablation. Compared to CVD, PLD is a transfer-free graphene synthesis. Bleu et al. achieved transfer-free graphene synthesis through nickel catalyst dewetting using rapid thermal annealing.[47] The graphene layers are formed on the top of the nickel film as well as at the contact between the film with the SiO_2 substrate due to the rapid diffusion of C across into the Ni film. The nickel dewetting process allows to expose the interfacial graphene and some graphene layers form agglomerates with nickel particle. Through the removal of nickel particles by an acid treatment, interfacial graphene was directly formed on the SiO_2 layer avoiding a time consuming and relatively complex transfer procedure. This research provides a possibility of layer controllable and transfer free graphene synthesis. The transfer of the graphene layer from the copper foil onto a substrate is necessary for CVD, which is typically conducted on thin copper foils. In such a transfer process, associated mechanical handling can result in corrugation and defects throughout the entire graphene layer as well as the potential for chemical residues, which adversely affect the graphene's intrinsic properties.

Not only graphene, but also graphene oxide (GO) and reduced graphene oxide (rGO), could be grown by PLD method. rGO has sparked much interest in applications that range from flexible optoelectronics, energy storage, sensing and as membranes to purify water. Large scale rGO films with high optical and electronic quality are required urgently by reproducible and scalable method. In 2020, as Figure 4d–f shows, Juvaid et al. have presented a one-step, scalable process to grow wafer-scale uniform thin films that resemble rGO using PLD of sp^2 carbon within an oxidizing atmosphere with ultrasmooth surfaces (roughness <1nm).[48] Compared to other methods grown rGO films, these films show better transparent and conductivity. Compared to chemical methods, this method does not use catalysts and are under low temperatures, which allows the integration of these thin films with other materials through direct growth. Bleu et al. made an initial endeavor to utilize solid precursors of carbon and boron, which were ablated by pulsed laser in a regulated manner (Figure 4g), to investigate the composition and nanostructure of films of B-doped graphene (BG).[49] The methodology is founded upon the co-deposition of PLD of carbon and boron, which has been previously explored for the purpose of acquiring uncontaminated graphene sheets.[50] They have already shown that PLD can be used to create carbon films that resemble diamonds and are doped with boron (a-C:B), which lays the groundwork for expanding the method for creating BG films proposed in this work. Contrary to what is typically seen with CVD synthesis, the PLD method revealed a similar boron content in the boron-doped carbon precursor and the finished boron-doped graphene, which is a significant benefit for the process reliability of doped graphene synthesis. Their study showed the ability of PLD to produce BG films and established a correlation between the synthesis process and the nanostructure and composition of the resulted films. For the purpose of achieving the desired composition and nanostructure of BG films in various electrical and electrochemical applications, the approach offers a new opportunity for B-doped graphene development using PLD in a controlled and repeatable manner.

From a solid-state carbon source, Wang et al. reported an effective method to prepare monolayer and bilayer graphene.[51] The growth of graphene can be modulated through the manipulation of laser energy density. The schematic diagram of the process for growing a graphene film is depicted in Figure 4h. A laser operating at KrF with a wavelength of 248 nm, corresponding to a photon energy of 5 eV, was employed to perform ablation on a target composed of highly oriented pyrolytic graphite (HOPG). The HOPG target has C—C bonds with an energy of 3.7 eV, and at 5 eV, the laser excitation causes the C—C bonds to shatter. Upon impact of the laser pulse with the target surface, a substantial quantity of carbon atoms was produced and propelled toward the substrate. A TEM characterization of the monolayer film is displayed in Figure 4i. The visual representation illustrates that the film is devoid of any visible impurities and possesses a smooth, even surface. The monolayer graphene has good crystallinity, as evidenced by the HRTEM image, which clearly demonstrates a regular arrangement. The SAED patterns are comparable to those from samples grown using CVD. With a laser energy density of 5.66 J cm^2, PLD can therefore be used to grow monolayer graphene films. Additionally, PLD is done in a liquid environment, which has its own benefits. Juvaid et al. published a study in 2020 about a novel single-stage synthesis method for bilayer graphene that uses excimer laser ablation of a commercially available graphite target in the DI water medium, making this method more affordable and practical for device applications.[52] This method allowed for the successful one-step laser ablation synthesis of high-quality bilayer graphene in DI water. **Table 1** underscore the numerous benefits of utilizing PLD technology in contrast to alternative methods. **Table 2** displays a summary of the experimental specifics of PLD graphene growth. These advantages include rapid growth rates, cost-effectiveness, the ability to control thickness and morphology primarily through the substrate, low growth temperatures, and the capacity to deposit composite thin films with intricate compositions by employing multiple targets to execute co-ablation in a managed and replicable manner. Additionally, when comparing graphene PLD growth to CVD, PLD requires a solid carbon target while CVD does not,

Table 1. Comparison of techniques used to realize 2D materials.

Method	Size	Throughput	Thickness Homogeneity	Fabrication Rate	Process Temperature	Reference
Mechanical exfoliation	560 mm × 600 mm	Low yield	Monolayer	Fast	Room temperature	ACS Nano, 2015, 9, 10612–10620
Liquid exfoliation	16.8 um	Low yield	Monolayer	Slow	–	Adv. Mater. 2019, 31, 1900568
CVD	20 um	Low yield	1 to *N*-layers	Slow	320 or 400 °C	Nat. Commun. 2019, 10, 4728
ALD	Wafer-scale	Low yield	4 nm	Slow	100 °C	Nat. Electron., 2022, 5, 849–858
MBE	Large-scale	Low yield	1 to *N*-layers	Slow	350 °C	NPJ 2D Mater. Appl., 2022, 6, 10
Thermal sputtering	Wafer-scale	High yield	2-3 layers	0.5 A s^{-1}	1000 °C	Nanoscale, 2012, 4, 6637
Magnetron sputtering	Wafer-scale	High yield	RMS roughness <0.2 nm	–	> 700 °C	Nanoscale, 2015, 7, 2497
PLD	Wafer-scale	High yield	Ra = 0.865 nm	85 nm h^{-1}	600 °C	Adv. Electron. Mater., 2022, 8, 12, 2022580

limiting the carbon source during segregation to that supplied during target ablation. Due to the fact that PLD grows graphene on a solid substrate, it can be handled more mechanically and offers an alternative method for controlling thickness at 0.1 A/pulse to CVD, where control is achieved by controlling gas pressure rather than laser power.

Applications of graphene produced by PLD are photo-diode, electrodes, p-type rGO electronics, and no transfer process compared to CVD. The ability to detect infrared rays for the purpose of sensing is crucial to modern world. One of the main challenges in the detection of infrared light is the difficulty in implementing Schottky contacts to narrow band gap semiconductors because of their surface and interface characteristics. In 2019, Apicella et al. got an extended Schottky multilayer-graphene/silicon junction as a lateral infrared photo-diode (**Figure 5**a).[53] A multilayer graphene layer was grown on an intrinsic silicon substrate. The film exhibits graphene near the interface and would transform into amorphous carbon when thickens. Here amorphous carbon behaves similarly to metal, forming a functional metallic/2D/Si heterostructure and exhibiting a rectifying behavior for *I*–*V* test. This study illustrates that PLD graphene is a good choice to broaden the spectrum of silicon applications. PLD graphene not only could be used as diode, but also as contact electrode in electronics. Goswami et al. got PLD NiO thin film and that was trapped in two conducting PLD graphene films (Figure 5c).[54] The graphene films here acted as contact electrodes for variation of electrical resistance under different temperature, shown that this system would be used as resistive random-access memory (RRAM), electric-switch and magnetic-switch. In addition, rGO by PLD method also shows promising electronic application. In 2020, Juvaid et al. got large scale rGO thin films via PLD method, tailored its hybrid sp^2-sp^3 electronic structure under situ control of the PLD growth environment (Figure 5d).[48] This allows control of its optoelectronic properties intrinsically and helps achieve some of the smallest extinction coefficients as well as refractive indexes (0.358 and 1.715 respectively, at 2.236 eV) when compared to rGO fabricated chemically. Gupta et al. shows the influence on free-electron carrier density in PLD rGO through changing the laser energy densities during laser annealing (Figure 5f).[55] They also reported on modulation of electron mobility within the liquid phase grown GO.

4. 2D Hexagonal Boron Nitrides (h-BN) Layers Produced Using PLD

The unique properties of hexagonal boron nitride (h-BN) include a large bandgap, a high thermal conductivity, a low dielectric constant, a significant band-edge absorption coefficient, and a high degree of chemical and thermal stability.[56–59] The PLD technique for creating h-BN layers is explored in this subsection. We will present a deeper understanding of how the benefits of PLD may be used to fabricate high-quality h-BN layers that preserve the unique features of this 2D material as we delve into the specifics of this technique. For 2D-based devices, h-BN is excellent as a gate dielectric, substrate, encapsulating layer, and tunneling barrier because of its layered structure and atomically smooth surface, which is free of dangling bonds and charge traps.[60–64] CVD method has been widely used to synthesize large-area h-BN films on a variety of substrates, including

Table 2. Summary of some of recent PLD grown graphene on various substrates.

Year	Structure	Growth Temperature	Base Pressure	Laser Energy	Background Gases	Morphology	Optical/Electrical Properties	Reference
2010	Graphene/Ni/n-Si	750 °C	5×10^{-6} Torr	50 mJ	–	–	Less defects	Appl. Phys. Lett., 2010, 97, 114102
2011	Graphene/Si	RT	10^{-5} Torr	5.0 J cm^{-2}	argon gas to 1 Torr	Ultrathin morphology	Few-layer graphene	Appl. Phys. Lett., 2011, 98, 173108
2011	Graphene/Ni/SiO_2/Si	650 °C	2×10^{-6} Torr	5.43 J cm^{-2}	–	Bi-, tri-, and few-layer graphene	–	AIP Advances, 2011, 1, 022141
2013	SiO_2/Si, SiN_x/Si, and p-Si substrates	900 °C	less than 10^{-8} mbar	3, 5, and 6 J cm^{-2}	high purity (5 N) argon gas	–	Electrical resistivity decrease	Appl. Phys. Lett., 2013, 102, 012110
2013	Graphene/Ni/SiO_2/Si	1010 °C	$5\text{-}6 \times 10^{-7}$ Torr	–	4 mTorr argon gas	Transfer-free monolayer and bilayer graphene on SiO_2	–	Appl. Phys. Lett., 2013, 103, 134102
2014	Graphene/fused silica	from RT to 700 °C	10^{-6} mbar	5 J cm^{-2}	0.1 mbar of oxygen	The formation of less than five layers of graphene	–	Appl. Surf. Sci., 2014, 317, 1004–1009
2014	Quartz, sapphire, and n-silicon substrates	750 °C	10^{-5} mbar	4 J cm^{-2}	10 Pa high purity (5 N) argon gas	Scalable graphene and controllable thickness	The optical transmittance and conductivity are comparable with exfoliated or metal-catalyzed graphene	Laser Phys. Lett. 2014, 11, 096001
2017	Graphene/Cu	500 °C	10^{-5} Torr	50 mJ pulse^{-1}	–	Different multi-layers	High quality	J. Appl. Phys., 2017, 121, 025303
2017	RGO/SiO_2/Si	700 °C	1×10^{-5} Torr	2 J cm^{-2}	oxygen pressure	Large area reduced graphene oxide (RGO) thin films grown	A very large carrier mobility of 372 cm^{-2} V^{-1} s^{-1}	J Material Sci. Eng. 2017, 6, 4
2018	Reduced graphene oxide	700 °C	10^{-4} mbar	3 J cm^{-2}	enough O_2, H_2O, and hydrogen molecules	RGO thin films fabricated	Maximum mobility was 1596 cm^{-2} vs^{-1}	IEEE Trans. Semicond. Manuf. 2018,31, 4, 535–544
2018	RGO/SiO_2/Si	700 °C	1×10^{-5} mbar	2 J cm^{-2}	O_2 gas	The greater inhomogeneity in the PLD grown wafer-scale RGO thin films	The temperature-dependent (5–400 K) electrical characterization of the thin films shows two distinct transport regimes	IEEE Trans. Magn. 2018, 54, 12, 1–9
2018	Graphene/SiO_2 substrate	780 °C	10^{-4} Pa	5 J cm^{-2}	N_2 gas at pressures of 0.5, 1 and 10 Pa during laser irradiation	2-3% nitrogen-doped 'few-layer' graphene	–	Sci. Rep. 2018, 8, 3247

(*Continued*)

Table 2. (Continued)

Year	Structure	Growth Temperature	Base Pressure	Laser Energy	Background Gases	Morphology	Optical/Electrical Properties	Reference
2019	Graphene/Ni/SiO_2/Si	1010 °C	5-6 × 10^{-7} Torr	75 mJ	–	Uniform deposition of carbon	High quality bilayer graphene	Phys. Chem. Chem. Phys., 2019, 238, 121905
2019	Graphene/Ni/Glass	750 °C	10^{-5} Torr	3.18 J cm^{-2}	30 sccm Ar flow rate	Formation of graphene domain	Increased crystallinity of graphene film	Results Phys., 2019, 14, 102350
2019	Ni/a-C:N/SiO_2	500 °C	10^{-5} Torr	5 J cm^{-2}	N_2 gas	Epitaxial monolayer to bilayer and rotated graphene	A high defective graphene-like structure	Carbon, 2019, 155, 410–420
2019	Graphene/SiO_2/Si	700 °C	10^{-3} Pa	1.5 J cm^{-2}	–	One to few-layered nano-sized graphene	Low resistance (ρ = (0.1–1.5) × 10^{-3} Ω m)	Appl. Surf. Sci. 2019, 480, 323–329
2019	Graphene/Ni/SiO_2	1100 °C	10^{-4} Pa	2.7 J cm^{-2}	–	The production of 1–4 layers boron doped graphene films	Increases the concentration of defects in the films	Appl. Surf. Sci. 2020, 513, 145843
2019	Monolayer and bilayer graphene/single crystal Cu (111) substrates	1000 °C	2.0 × 10^{-6} Pa	5.66 J cm^{-2} 8.49 J cm^{-2}	–	The controllable growth of high-quality monolayer and bilayer graphene	–	Appl. Surf. Sci. 2019, 494, 651–658
2019	Graphene/Si or SiO_2/Si	from 600 to 1000 °C	10^{-4} Pa	4.5 J cm^{-2}	–	Mainly bilayer and trilayer graphene on SiO_2	–	J Raman Spectrosc. 2019, 50, 1630–1641
2019	Graphene/Si	550 °C	10^{-2} Torr	300 mJ	–	A multilayer-graphene/silicon infrared Schottky photodiode	Graphene increases the spectrum of absorbance of silicon	Adv. Electron. Mater. 2019, 5, 1900594
2020	rGO/Si	680 °C	0.5 mTorr	2.9 J cm^{-2}	oxygen	Wafer-scale uniform rGO-like thin films with ultrasmooth surfaces (roughness <1 nm)	Transparency and conductivity metrics are superior	ACS Nano 2020, 14, 3290–3298
2020	rGO/SiO_2/Si	300 K	10^{-6} Torr	3.5–4.0 J cm^{-2}	–	The electron mobility modulation in the liquid phase grown GO	26 cm^{-2}/Vs room-temperature electron mobility and -4.7 × 10^{21}/cc charge carrier concentration	Carbon 2020, 170, 327–337
2020	Graphene/SiO_2/Si	–	–	between 2.5 to 3.75 J cm^{-2}	–	DI water environment	Producing good quality bilayer graphene	Mater. Res. Bull. 2020, 126, 11840
2021	a-C/Ni/SiO_2	RT	10^{-7} mbar	5 J cm^{-2}	–	Transfer-free graphene synthesis	–	Appl. Surf. Sci. 2021, 555, 149492
2022	Graphene/NiO/Graphene	650 °C	10^{-6} Torr	450 mJ	Ar gas	Graphene as conducting electrode	–	

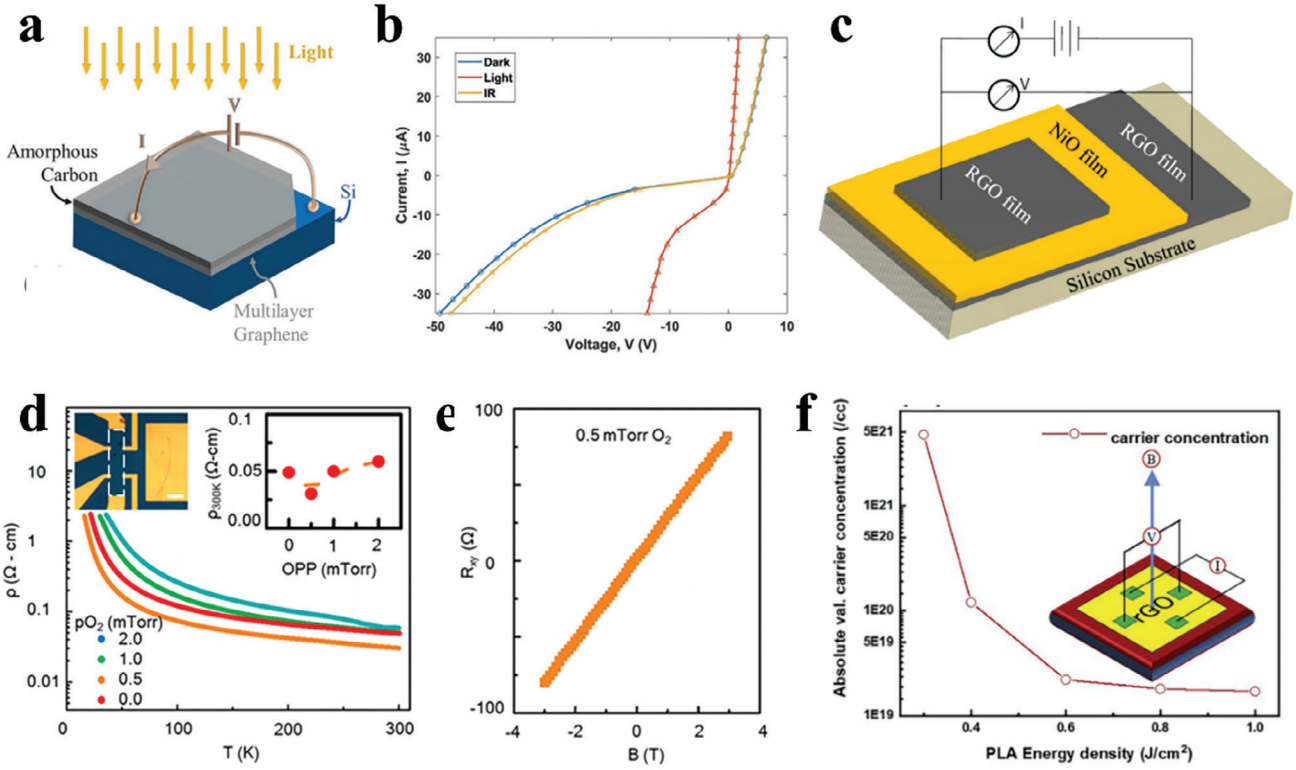

Figure 5. a) Sketch of the multilayer-graphene/silicon infrared Schottky photo-diode device. b) Current–voltage characteristics measured in dark, light and infrared. c) Schematic representation of the graphene-NiO-graphene film. d) Resistivity vs temperature plot for rGO-like films grown at different oxygen partial pressures. Inset: Optical image of patterned Hall bar device used for electrical transport measurements. The scale-bar is 100 μm. The red dots in the inset represent the room-temperature resistivity of the films grown at various OPPs, and the orange line is a guide to the eye. e) The slope of Hall resistance vs. magnetic field confirming p-type conduction in the films. f) The impact on free-electron carrier density in rGO on changing the energy densities during laser annealing. a,b) Reproduced with permission from ref. [53]. Copyright 2019, IPO Publishing. All rights reserved. c) Reproduced with permission from ref. [45]. Copyright 2022, IPO Publishing. All rights reserved. d,e) Reproduced with permission from ref. [48]. Copyright 2020, American Chemical Society. All rights reserved. f) Reproduced with permission from ref. [55]. Copyright 2020, Elsevier. All rights reserved.

Cu, Ni, and Fe, employing reactive precursors such as ammonia borane (H_3NBH_3) and borazine ($B_3N_3H_6$), which are poisonous, unstable, and flammable.[65–68] Also, degradation of h-BN occurs due to the introduction of contaminants and mechanical damage during the transfer process from metal substrates to a more appropriate surface (typically a dielectric substrate) for device fabrication. PLD is an alternative technique that can be utilized to synthesize high-quality h-BN with controllable thickness and large surface areas (**Figure 6a**).[69] Wang et al. in 2021 utilized PLD on non-catalytic sapphire substrates to directly synthesize high-quality h-BN films and thoroughly investigated the effects of the deposition parameters.[70] The photodetectors based on h-BN exhibit remarkable UV detection capability, as evidenced by their on/off ratio of $>10^4$ and photoresponsivity of up to 1.69 mA W^{-1}, as shown in Figure 6b and c, respectively. The temperature of the substrate had the most significant impact on the crystalline nature of the h-BN films of all the growth parameters they investigated, as shown by the gradual rise in photocurrent of over 400%, while the substrate temperature rises during the PLD process from 800 to 1250 °C. In 2023, Biswas et al. utilized PLD to directly deposit large-area h-BN thin films on c-cut sapphire substrates.[71] In contrary to previous reports,[68,72–74] h-BN films demonstrate unidirectional domain growth morphology without the need for a catalytic support. The UV–vis absorption spectrum of the h-BN film at room temperature revealed a prominent peak at 214 nm (Figure 6d).[71] Using the Tauc-plot, the bandgap was calculated to be ≈5.95 eV, in agreement with the previously reported value.[75] The valence band spectrum (VBS) of the XPS revealed the band structure of the h-BN film to contain two distinct features with binding energies of 12 and 20 eV, respectively. In addition, magnetic hysteresis (M-H) measurements at room temperature reveal a flawless diamagnetic response, indicating that the synthesized h-BN films are nearly devoid of flaws or impurities (Figure 6f).[71] They utilized no metal catalytic support and directly deposited 2D-vdW h-BN thin films by PLD on low-miscut, atomically smooth sapphire substrates to demonstrate unidirectional domain growth. The passivation of the nucleation sites along the preferred step-edge orientation of the substrate, which is responsible for the unidirectional domain growth, is revealed by their density functional theory (DFT) calculations. The mechanism involves a strong interaction between the film-substrate interfacial symmetry and energy. Various techniques for characterization have been employed to verify the development of h-BN films with superior intrinsic properties. Their discovery has the potential to facilitate the growth of high-quality thin films with unidirectional domains over a large area directly

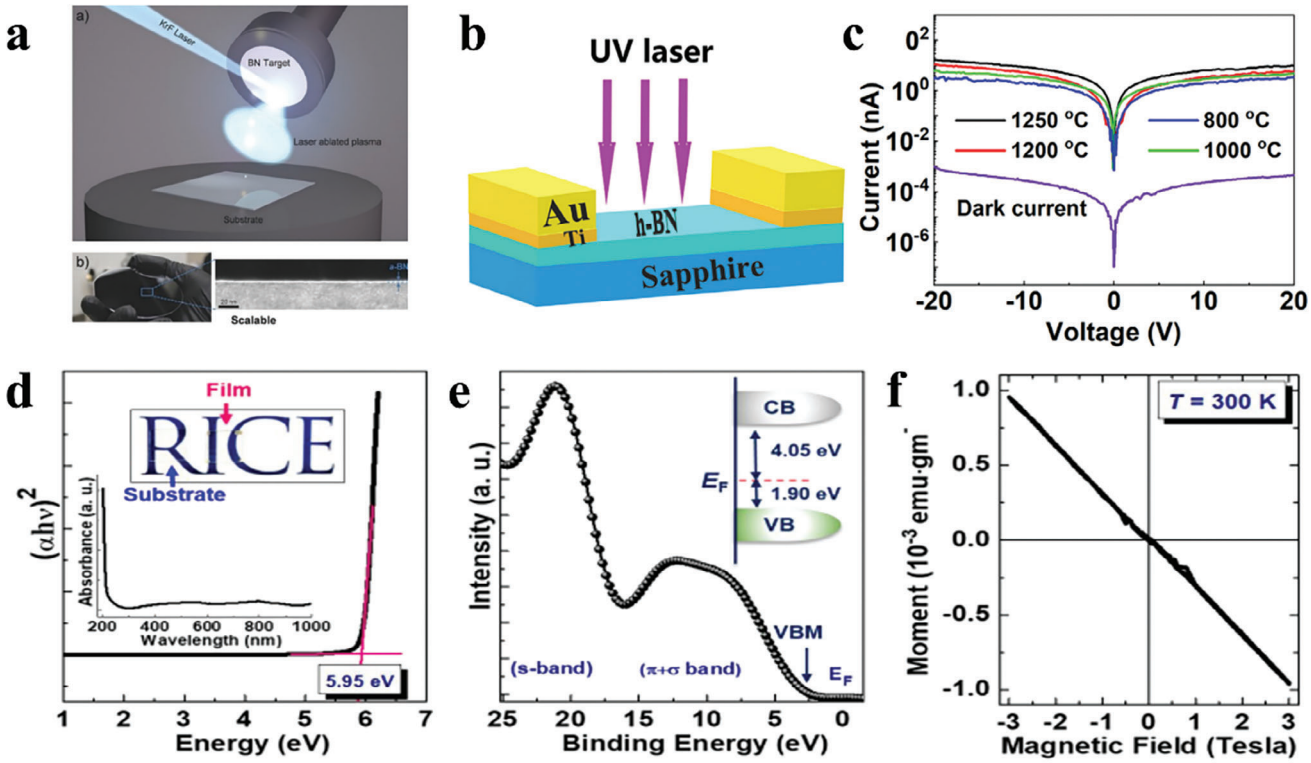

Figure 6. a) Up panel: Sketch of PLD growth of h-BN film. Down panel: Photo and SEM image of h-BN film on sapphire. b) A diagram of an h-BN UV photodetector. c) *I–V* curves of photodetectors constructed from h-BN films at various substrate temperatures. d) Spectra of UV-vis absorption and the fitting Tuac plot of the h-BN film. e) XPS spectrum of the h-BN film. f) Magnetization measurement of h-BN film. a) Reproduced with permission from ref. [69]. Copyright 2016, Wiley. All rights reserved. b,c) Reproduced with permission from ref. [70]. Copyright 2021, National Natural Science Foundation of China (NSFC). All rights reserved. d–f) Reproduced with permission from ref. [71]. Copyright 2023, Elsevier. All rights reserved.

on insulating substrates. This development could prove to be instrumental in advancing 2D electronics with superior performance. Furthermore, Ajayan et al. (2023) demonstrated a state-of-the-art approach in synthesizing h-BN nanosheets at ambient temperature using a highly energetic PLD growth technique, exhibiting outstanding functional features and usefulness for several applications.[76] **Table 3** provides a summary of several recent PLD-produced h-BN on different substrates.

5. 2D Black Phosphorus (BP) Layers Grown Using PLD

The unique properties of black phosphorus (BP) make it a highly desired 2D material due to its direct bandgap, which can be adjusted across a wide range of wavelengths from visible to infrared by increasing the number of layers, as well as its exceptional charge carrier mobility.[77,78] The controlled growth of few-layer BP films has been a significant challenge since the discovery of BP, impeding further exploration and practical applications. To date, the assembly of preferable BP thin films has primarily relied on bottom-up mechanical or chemical exfoliation techniques from bulk crystals.[79–81] This has resulted in the assembly of relatively diminutive thin layers, typically measuring 5–50 μm^2. In recent times, bottom-up methodologies, such as CVD techniques, have been utilized for the synthesis of few-layer BP.[82,83] However, the lateral dimensions of the obtained flakes were limited to only a few dozen micrometers. Recently, PLD has been a promising method to prepare high quality ultrathin BP films. There has been a successful achievement in the growth of 2D BP film on an ultra-flat mica substrate using the PLD technique, which has exhibited exceptional film quality. In 2015, Yang et al. obtained an amorphous BP thin film with a thickness of 2–10 nm with graphene/copper or SiO_2/Si substrates by PLD method (**Figure 7a**).[16] Compared with other film preparation techniques, the growth conditions are easier to realize and it is easier to obtain high quality thin films, which is in contrast to extreme conditions of high pressure or high temperature for growing BP phase in the previously reported publications. The number of laser pulses could roughly control the thickness of the films, and the quality of the amorphous BP thin films could be controlled by the substrate temperature. As Figure 7b shows, the fabricated 2 nm p-type a-BP thin film FET shows a moderate on/off current ratio (which is up to 10^2), and high field-effect mobility (which is up to 14 cm^2 V^{-1} s^{-1}).[16] In 2018, Qiu et al. proposed an innovative laser writing process-confined ultrafast pulsed laser deposition (CUPLD) (Figure 7c).[84] In this research work, they realized the large scale growth of directly synthesizing continuous BP thin films from high quality large bulk BP crystal with the capability of patterning arbitrary shapes by employing ultrafast laser writing with confinement. During the growth process, the ultrafast picosecond laser pulse could generate local high-temperature and high-pressure conditions for

Table 3. Summary of some of recent PLD grown h-BN on various substrates.

Year	Structure	Growth Temperature	Base Pressure	Laser Energy	Background Gases	Morphology	Optical/Electrical Properties	Reference
2016	$BN/SiO_2/Si$	Less than 200 °C	50 mTorr	22.5 J cm^{-2}	N_2 gas	Ultrathin amorphous boron nitride of thicknesses from 2 to 17 nm	A device-scale dielectric constant of 5.9 ± 0.65 at 1 kHz, breakdown voltage of 9.8 ± 1.0 MV cm^{-1}, and bandgap of 4.5 eV	Adv. Funct. Mater. 2016, 26, 2640–2647
2020	BN/Si	600 °C	1×10^{-3} Torr	2.4 mJ	–	PLD process to grow thick and adherent BN films	–	Mater. Res. Express, 2020, 7, 096401
2021	BN/Sapphire	800–1250 °C	3×10^{-7} Torr	300–700 mJ	N_2 gas	High-quality h-BN films with a controllable thickness on sapphire	Superior deep-ultraviolet detection performance with a large on/off ratio of $> 10^4$, high photoresponsivity, and a sharp cut-off wavelength of 220 nm	Fundam. res. 2021, 1, 677–683
2023	BN/Sapphire	800 °C	100 mTorr	2.2 J cm^{-2}	N_2 gas	Large area direct growth of electronic-quality h-BN thin films on insulating substrates	Dielectric layer and valence band maxima (VBM) at ≈1.9 eV	Appl. Mater. Today, 2023, 30, 101734

a few picoseconds through adopting a confined ultrafast laser setup, which is necessary for the metaphase transformation from ablated phosphorus to reconstructed BP thin films. Under this optimized laser intensity, a crystalline BP thin film appears on the substrate through a metaphase transformation. Compared to traditional PLD method, CUPLD could get specific graphics (Figure 7d). In addition, the researchers induced molecular dynamics (MD) simulation to explain the physical mechanism of confined laser metaphase transformation. Finally, BP field-effect transistors show excellent electrical properties. This novel laser direct writing method could provide a fast route to prepare large-scale BP ultrathin films, meanwhile this one-step pattering process could provide a potential possibility that can be applied to other 2D materials. One of the most attractive features of this method is a one-step process, which integrates ablation, deposition and patterning continuously. The CUPLD is an intriguing and fast route for massive nanomanufacturing. In 2019, Bellus et al. introduced an amorphous semiconductor to the material library for constructing van der Waals heterostructures and fabricated heterostructures composed of a 2 nm amorphous PLD BP layer and a monolayer of WS_2 (Figure 7e).[85] Their findings indicate that the transfer of holes from WS_2 to amorphous BP occurs rapidly, as demonstrated by both time-integrated PL and time-resolved transient absorption measurements.

In 2021, Wu et al. demonstrated the controlled PLD method for achieving high-quality, large-scale growth of a few-layer 2D BP. The authors describe a methodical approach utilizing PLD to produce superior quality BP ranging from monolayer to few-layer thicknesses on a scale of centimeters, as depicted in Figure 7h. The laser ablation-induced plasma-activated region offers favorable circumstances for forming and transporting BP clusters, thereby promoting growth (as depicted in Figure 7f).[15] During the PLD process, bulk monocrystal BP work as the source and mica work as substrate under an ultrahigh vacuum chamber. The as-grown BP films exhibit a distinct reflective color in contrast to the bare mica. This uniform sheen is observed to extend over the entire 1 cm^2 surface of the mica wafer, as depicted in Figure 7g.[15] The utilization of pulsed laser in lieu of conventional heat-assisted evaporation has been demonstrated to promote the formation of significant BP clusters within the transported physical vapor, thereby reducing the formation energy of the BP phase and enabling the large-scale growth of few-layer BP, as evidenced by the results obtained from MD simulations. The authors have successfully demonstrated the homogeneity of the obtained BP over a large area, as depicted in Figure 7i. Furthermore, they have made significant progress by creating centimeter-scale FET arrays based on BP film, which exhibit impressive electrical performances that are comparable to those of previously reported micrometer-scale BP. The uniformity of the electrical performances across the entire film is crucial for the development of BP-based semiconductor integrated circuits in the information industry. The hole mobility of the BP-based semiconductor integrated circuits is up to 213 and 617 $cm^2\ V^{-1}\ s^{-1}$ at 295 and 250 K, respectively, as illustrated in Figure 7j,k.

By employing the PLD technique, it was possible to cultivate large-scale, few-layer BP films with lateral dimensions that

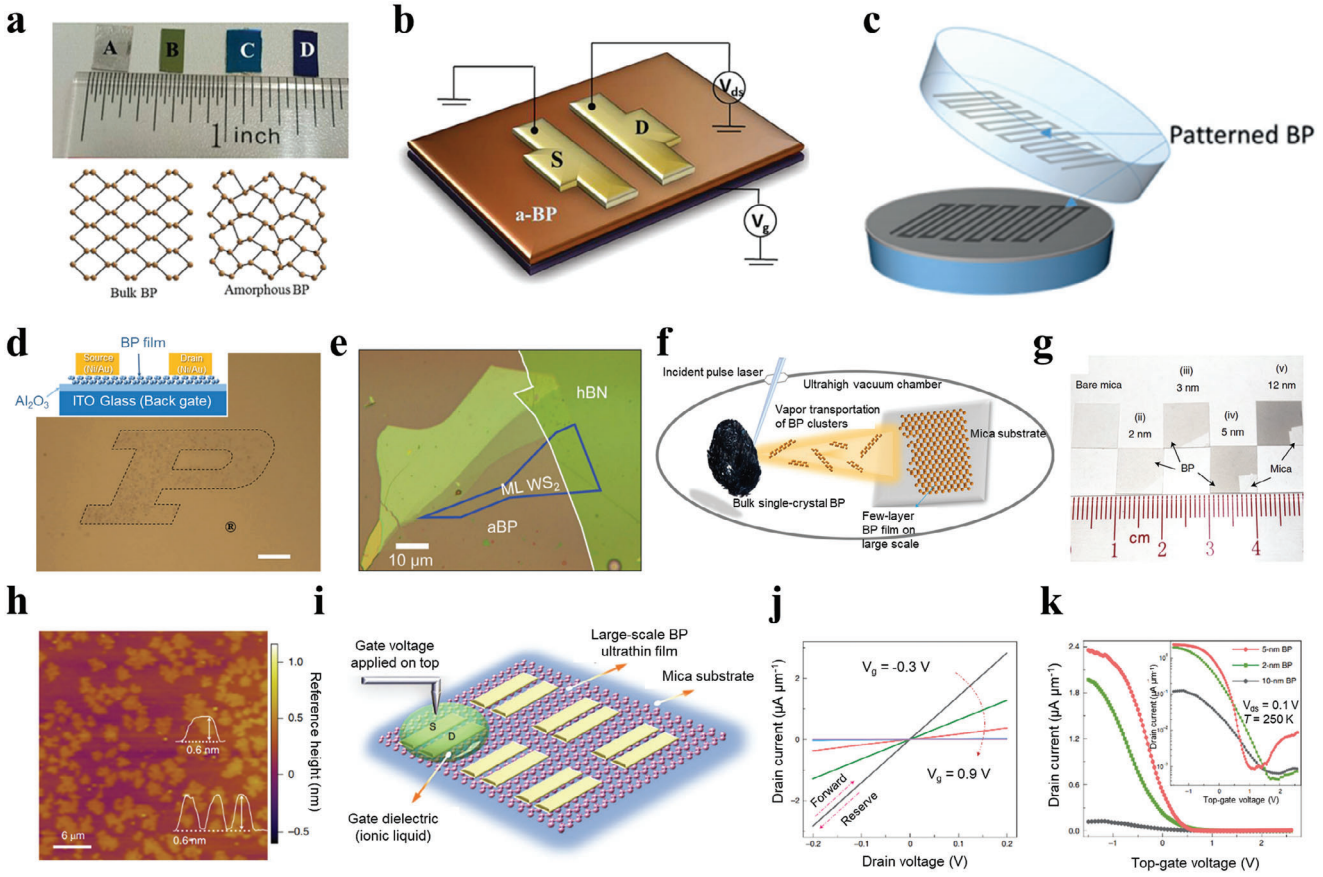

Figure 7. a) Up panel: Photographs of BP films deposited under different conditions (from left to right: film/graphene/copper deposited at 150 °C; film/SiO_2/Si deposited at 150 °C; film/SiO_2/Si deposited at 250 °C; film/SiO_2/Si deposited at 300 °C). Down panel: Schematic of top-view atomic models of BP crystal and α-BP. b) Schematic illustration of FET device based on PLD grown a-BP ultrathin film. c) Large-scale patterned BP thin films by ultrafast laser direct writing. d) An optical image of a BP thin film patterned into the shape of P. The scale bar is 10 μm. e) Optical images of the WS_2/PLD-αBP heterojunction. f) Schematic of the PLD process for growth of centimeter-scale few-layer BP films. g) Photographs of bare mica i) and as-deposited centimeter-scale BP films of different thickness ii–v). h) AFM image of monolayer BP flakes. The monolayer thickness is indicated by the inserted height profile. i) Schematic of arrayed top-gated FETs based on centimeter-scale few-layer BP grown on mica substrate. j) Drain current–drain voltage (I_d–V_{ds}) curves for a FET based on a 5-nm BP ultrathin film under different gate voltages (V_g) at 250 K. k) Transfer characteristics of FETs based on 2-, 5- and 10-nm BP ultrathin films in linear scale at 250 K. The inset shows the same results in a logarithmic scale. a,b) Reproduced with permission from ref. [16]. Copyright 2015, WILEY-VCH Verlag GmbH & Co. KGaA. All rights reserved. c,d) Reproduced with permission from ref. [84]. Copyright 2018, WILEY-VCH Verlag GmbH & Co. KGaA. All rights reserved. e) Reproduced with permission from ref. [85]. Copyright 2019, Royal Society of Chemistry (RSC). All rights reserved. f–k) Reproduced with permission from ref. [15]. Copyright 2021, Nature Publishing Group (NPG). All rights reserved.

surpass those reported in prior studies. These dimensions ranged from several micrometers to the centimeter scale. The technology used for preparing PLD films exhibits various advantageous characteristics for the purpose of device fabrication. The advantages encompassed in this context include meticulous regulation of film thickness, stringent stoichiometric growth, expeditious growth rate, exceptional compatibility with multilayered heterostructures, and cost-efficiency. The utilization of PLD technology, in contrast to other methods such as CVD, mechanical exfoliation, and liquid phase method, could lead to the development of wafer-scale BP electronic and optoelectronic devices, including scalable integrated device arrays and information systems. These devices would be larger in size compared to BP nanosheets produced through other techniques. PLD technology is a viable option for creating wafer-scale BP electrical and optoelectronic devices, which encompasses the possibility of creating expandable arrays of integrated devices and information systems. **Table 4** provides an overview of recent PLD-produced BP on varied substrates.

6. 2D Transition-Metal Dichalcogenides (TMD) Films Grown Using PLD

In the emerging fields of spintronics and valleytronics, which encompass various microelectronic devices, TMDs have recently demonstrated their potential for usage in intriguing ways.[86–91] Although CVD and exfoliation methods are frequently used to produce high-quality monolayers and multilayers sheets of 2D TMDs, nevertheless, the unpredictable nucleation during CVD synthesis and microscopic flake shape hinder their practical device applications. Also, mechanical exfoliation approach lacks exact control over the exfoliated surface, morphology, thickness,

Table 4. Summary of some of recent PLD grown BP on various substrates.

Year	Structure	Growth Temperature	Base Pressure	Laser Energy	Background Gases	Morphology	Optical/Electrical Properties	Reference
2015	Graphene/copper or SiO_2/Si substrates	150 °C	1.5×10^{-7} Torr	–	–	2 nm wafer scale	p-type transistor behavior, a moderate on/off current ratio up to 10^2, and high field-effect mobility up to 14 cm^{-2} V s	Adv. Mater. 2015, 27, 3748–3754
2018	Sapphire, quartz, PET, etc.	750 °C	0.01 mTorr	–	–	Mass produce large-scale patterned BP films with a one-step manufacturing process	p-MOSFET behavior with on/off ratio on the order of 10	Adv. Mater. 2018, 30, 1704405
2019	Si/SiO_2	150 °C	1.5×10^{-7} Torr	–	–	2 nm amorphous BP synthesized	Introduce an amorphous semiconductor to the material library for constructing van der Waals heterostructures	Nanoscale Horiz., 2019, 4, 236–242
2021	Mica	300 °C	1.6×10^{-9} Torr	1.2 J cm^{-2}	N_2 gas	The growth of ultrathin single crystal BP on the centimeter scale	Few-layer BP FETs exhibits appealing electrical characteristics in terms of carrier mobility and current switching ratio	Nat. Mater. 2021, 20, 1203-1209

and layer uniformity. PLD has been shown to be an efficient technique for producing high-quality, homogenous, and stoichiometric thin films that are excellent for device fabrication. Serna et al. reported the PLD synthesis of a few layers of MoS_2 films with high crystallinity over broad areas on sapphire, HfO_2, and SiO_2 substrates with no prior pre-surface treatment.[92] Besides the tiny wafer edges that were hung on the substrate holder during deposition, the whole sapphire wafer was uniformly covered with MoS_2 film (**Figure** 8a). Raman spectra were obtained from the top, bottom, left side, right side, and middle of the same substrate. The presence of the E^1_{2g} and A_{1g} vibration modes evidenced the presence of the MoS_2 thin layer all over the sapphire substrate. In addition, to learn more about the electrical transport mechanism, they measured resistivity and found that it was $\approx 1.54 \times 10^4$ Ω cm^{-1} for the 1:2 Mo:S stoichiometric ratio, as shown in Figure 8b. Kumar et al. fabricated an array (Figure 8c) of highly sensitive and efficient MoS_2-based UV photodetectors grown using the PLD technique. At a low applied bias voltage, the photodetectors displayed remarkable device performance.[93] The obtained results are stimulating in terms of attaining low power consumption and highly efficient MoS_2-based UV photodetectors. Many studies show that WS_2 is comparable to MoS_2 and has better thermal stability and optical properties.[94,95] Because of the heavy tungsten atom in WS_2, significant spin-orbit coupling and extensive band-edge spin splitting may occur, making it a possible candidate for spintronic and valleytronics devices.[96,97] Recent research has shown that the CVD method is best for synthesizing 2D WS_2 films with a large surface area. However, due to high deposition temperatures (>800 °C), complex gas flow setup, and health hazards, this technique is unsuitable for large-scale production.[98] Kun et al. utilized PLD to grow WS_2 monolayer films on large areas of sapphire substrate with a high degree of uniformity.[99] Figure 8d depicts AFM imaging and the height profile between the substrate and the as-grown WS_2 film. According to the AFM profile, the height of the film is roughly 0.7 nm, which is in line with the monolayer thickness of WS_2. According to the root-mean-square estimations, the roughness is found to be 0.4 nm. Furthermore, Godel and coworkers utilized the PLD technique to fabricate a large-scale 2D sheet of WS_2 on both ferromagnetic spin source substrates (Ni) and dielectric substrates ($SrTiO_3$), which were required for spintronic systems and in-plane semiconductor circuit frameworks, respectively.[100] Figure 8e shows the typical current $I(V)$ and its first derivative dI/dV for vertical tunneling transport measurements that were measured at 4 K. The tunneling effect was observable in both the $I(V)$ and dI/dV curves. Zheng and coworkers exploit

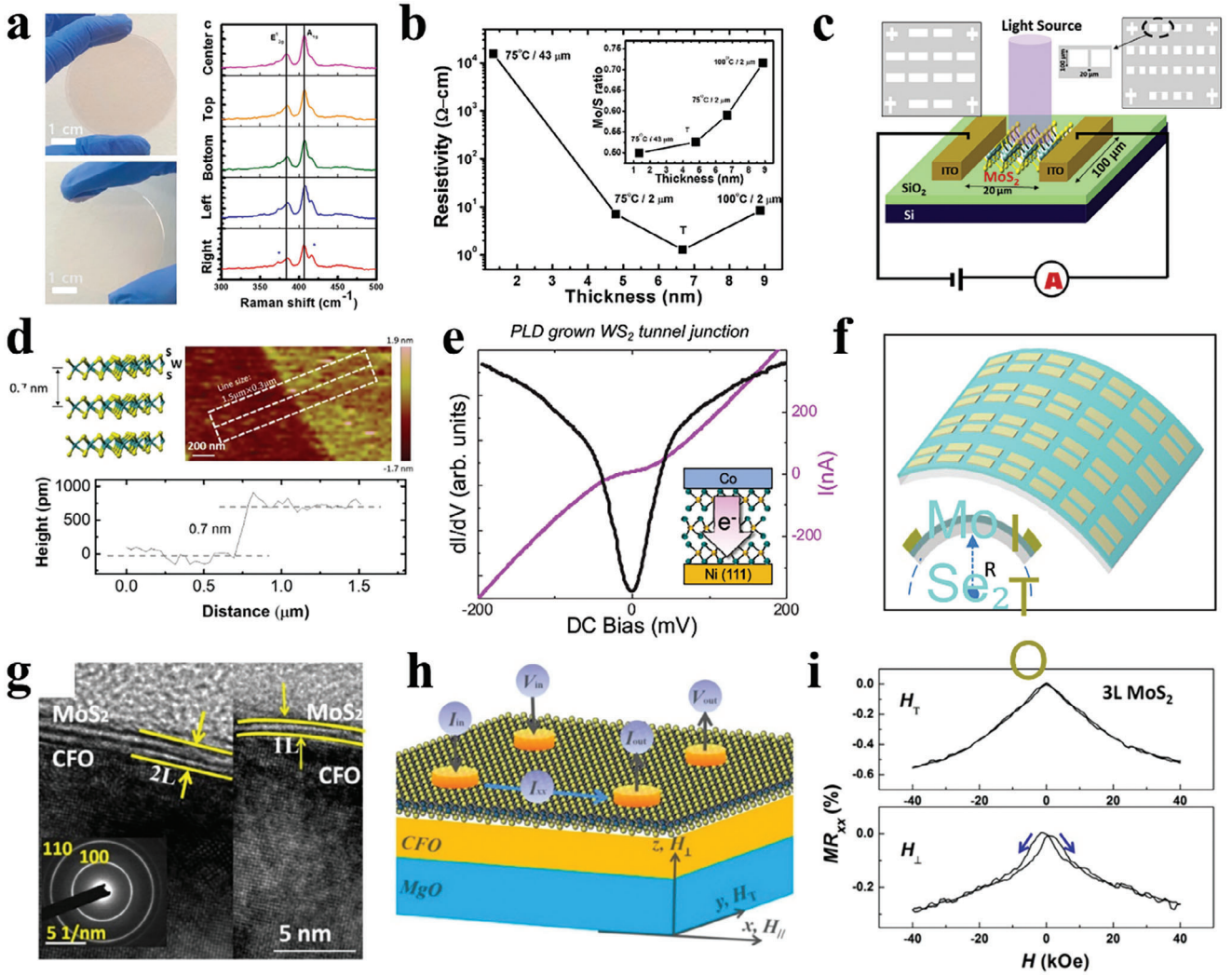

Figure 8. a) Left: photos of PLD-deposited bilayer MoS_2 thin film. and Raman spectra at various points on a 2-in diameter Al_2O_3 wafer. b) Resistivity of MoS_2 thin films with various Mo/S atomic ratios. c) Illustration of a mass-produced MoS_2-based photodetector. d) AFM image and thickness profile of monolayer PLD-grown WS_2 film. e) dI/dV characterizations of the Ni/WS_2/Co heterostructures. f) Schematic of flexible WSe_2 photodetectors and curvature radius definition. g) TEM images of MoS_2/CFO heterostructures with 2L and 1L MoS_2 layers. h) MoS_2/CFO heterostructure with van der Pauw geometry schematics. (i) MR behaviors of 1L MoS_2 at 300, 150, and 100 K. a,b) Reproduced with permission from ref. [92]. Copyright 2016, American Chemical Society. All rights reserved. c) Reproduced with permission from ref. [93]. Copyright 2020, Elsevier. All rights reserved. d) Reproduced with permission from ref. [99]. Copyright 2018, Elsevier. All rights reserved. e) Reproduced with permission from ref. [100]. Copyright 2020, American Chemical Society. All rights reserved. f) Reproduced with permission from ref. [101]. Copyright 2016, IOP Publishing Ltd. All rights reserved. g–i) Reproduced with permission from ref. [102]. Copyright 2017, American Chemical Society. All rights reserved.

the versatility of PLD techniques to grow large-area, highly crystalline 2D nanosheets of WSe_2 films in order to make an assembly (Figure 8f) of flexible, transparent, highly stable, ultrabroadband (370 to 1064 nm), photodetectors with high responsiveness and sensitivity.[101] Jie et al. investigated the effects of spin-orbit coupling that led to magnetoresistance (MR) in heterostructures of insulating ferromagnetic $CoFe_2O_4$ (CFO) thin films and PLD-grown MoS_2 layer at ambient temperature.[102] Figure 8g shows cross-sectional HRTEM images demonstrating the layered nature of PLD-grown MoS_2 and the CFO-MoS_2 interface. Figure 8h shows how to measure the longitudinal resistance of 1L MoS_2 with expected anisotropic MR. The anisotropic MR reduces gradually as temperature falls from 300 to 100 K, as depicted in Figure 8i. Based on wafer-scale MoS_2/CFO heterostructures, their findings could aid in developing 2D ultrathin data storage devices at ambient temperature.

Microelectronic device performance, however, is sensitive to band alignment and band offset values at the interface between materials.[103] 2D heterojunctions are of interest for optoelectronics and quantum-well systems due to the band alignment at the heterointerface. In order to reduce the amount of leakage current in electro-optical systems, larger band offset values are generally preferred. Therefore, the values of band alignment and band offset at the 2D heterojunction are critical to the functionality of micro-devices. Sinha et al. carried out a thorough investigation of band alignment in PLD-grown large-area MoS_2/SiO_2

Table 5. Summary of deposition conditions and properties of TMDs nanosheets by PLD.

Year	Structure	Growth Temperature (^{0}C)	Base Pressure (Torr)	Laser Energy (J/cm^{-2})	Background Gases	Morphology	Optical/Electrical Properties	Reference
2015	$WS_2/SiO_2/Si$	500	1×10^{-4}	–	Ar	Continuous WS_2 film with lateral size of one cm	Optical absorbance of 40%–85% and high carrier mobility of 31 cm^{-2} V s	Nanoscale, 2015, 7, 14974–14981
2017	MoS_2/CFO	650	3.6×10^{-7}	250 mJ and the pulse frequency of 1 Hz	–	Large area 1L and ML MoS_2	RT magnetoresistance of -12% of 1L MoS_2	ACS Nano, 2017, 11, 7, 6950–6958
2019	MoS_2/Au(111)	500	7.5×10^{-12}	1.5	None	Large-area single layer MoS_2	Au suppressed excitonic emission of 1L MoS_2	Nanoscale Adv., 2019, 1, 643–655
2019	ReS_2/MoS_2 (001)/Al_2O_3 (0001)	400-900	1.33×10^{-3}	–	N_2	Large area epitaxial (10×10 mm^2) growth of ReS_2	Truncated ReS_2 thin films possess optical emission peaks corresponding to both monolayer and multilayer	Thin Solid Films, 2019, 685, 81–87
2020	WS_2/Ni (111) $WS_2/SrTiO_3$	450, 600	1×10^{-3}	80 mJ 2.5 Hz	Ar	Wafer-scale homogeneous monolayer layer of WS_2	WS_2/Ni electrode exhibited resistant to oxidation and good tunneling features	ACS Appl. Nano Mater., 2020, 3, 8, 7908–7916
2021	MoS_2/SiO_2	600–800	1×10^{-6}	1.2	N_2	Centimeter scale monolayer MoS_2 with a uniform surface	High I_{ON}/I_{OFF} ratio of 10^5, relatively high mobility of 44.6 cm^{-2} V s	Mater. Sci. Eng. B 2021, 266, 115047
2021	MoS_2/SiO_2	800	1×10^{-6}	–	N_2	Large-area single layer MoS_2	Direct bandgap of monolayer MoS_2 found E_g = 1.85 eV (direct)	J Appl. Phys, 2021, 129, 115303
2021	MoS_2/SiO_2	700	1×10^{-6}	2	None	Polycrystalline 1L and 2L of MoS_2	The bilayers MoS_2 exhibit AB and AA′ stacking orientations	ACS Nano 2021, 15, 2, 2858–2868

heterostructures and, consequently, band offset values (CBO and VBO) at the heterojunction as a function of the number of MoS_2 layers changes dramatically.[104] As the number of layers increases, they notice that the valence- and conduction-band offsets (VBO and CBO) at the MoS_2/SiO_2 heterojunction are getting bigger. Their results can be explained by the fact that denser MoS_2 films experience a shift in the Mo-4d orbital due to interlayer coupling, causing a decrease in its bandgap and thus expanding VBO and CBO values. Furthermore, $ZnIn_2S_4$ (ZIS) is a layered ternary compound with a direct and modifiable bandgap, high light harvesting efficiency, excellent chemical stability, and low environmental impact.[105–107] The beneficial features of ZIS make it an attractive candidate for use as a photocatalysis and photo sensing material.[108] Despite its many advantages, a high-quality, large-area 2D form of ZIS rarely exists in the literature until Ye et al. report in 2022.[109] Their work reveals that the PLD technique could be utilized to synthesize centimeter-scale, homogeneous, high-quality ultrathin ZIS crystals. ZIS-based photodetectors exhibit excellent photosensitivity with an on/off switching ratio exceeding 10^3 under 405 nm illumination. The device photo response

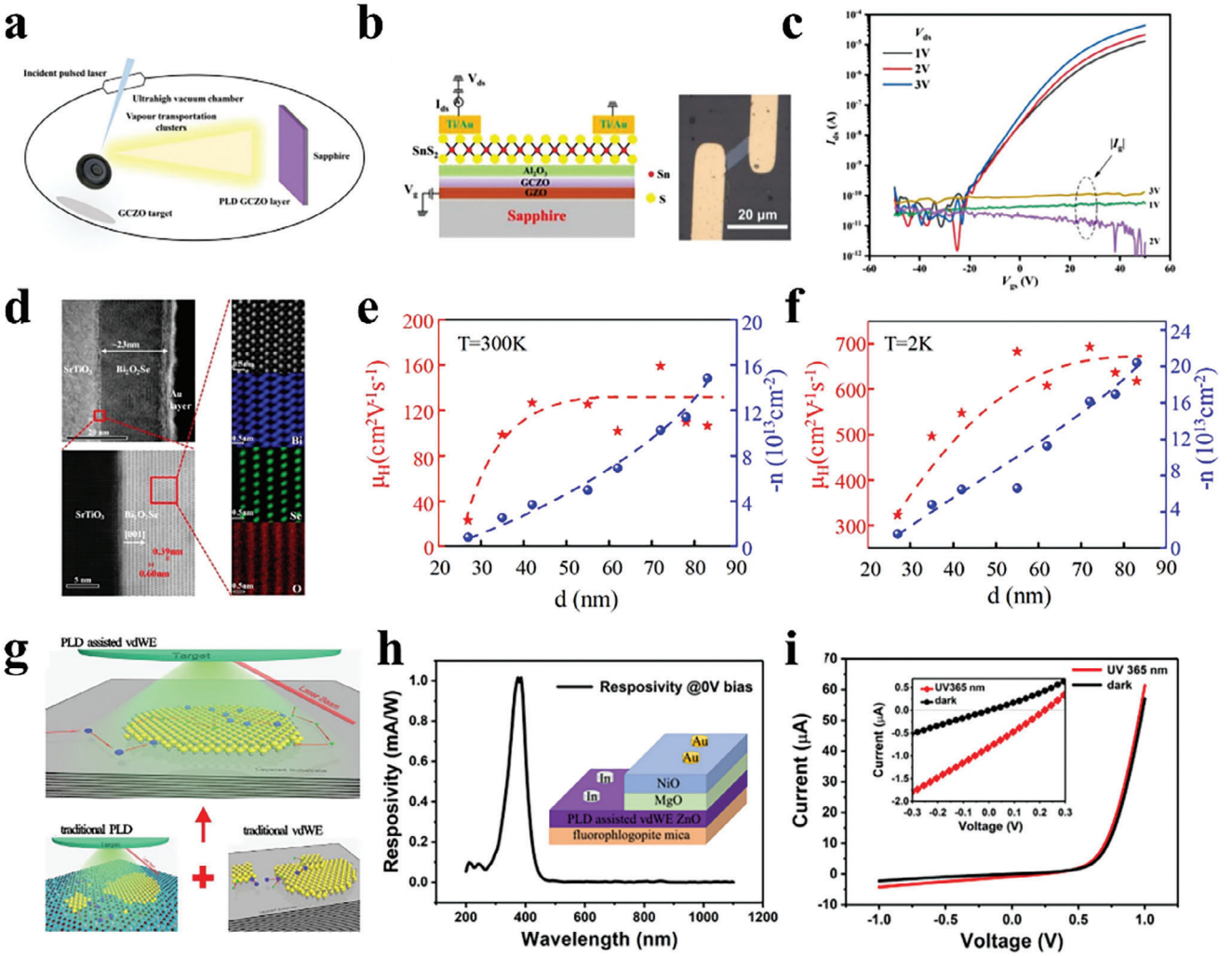

Figure 9. a) Schematic diagram of the typical PLD technique. b) Left panel: Schematic cross-section of a SnS_2-based FET device on a GCZO dielectric. Right panel: Optical image of the corresponding device. c) In log scale, transfer characteristics with varying bias voltage. d) Cross-sectional low and HR-TEM image of the Bi_2O_2Se film and corresponding EDX mapping of Bi, O, Se elemental composition. e,f) Statistics and comparison of Hall mobility and carrier concentration as a function of the Bi_2O_2Se film thickness at 300 K e) and 2 K f). g) Schematic diagram of the vdW-assisted PLD methods. h) A p-NiO/i-MgO/n-ZnO photodetector response spectrum. The design of the photodetectors is depicted in the inset. i) The *I*–*V* curves in the dark and under UV 365 nm light irradiation. a–c) Reproduced with permission from ref. [23]. Copyright 2022, Wiley-VCH. All rights reserved. d–f) Reproduced with permission from ref. [118]. Copyright 2020, IOP Publishing Ltd. All rights reserved. g–i) Reproduced with permission from ref. [117]. Copyright 2019, Wiley-VCH. All rights reserved.

improves with channel thickness, reaching photoresponsivity of 1.4 A W^{-1}, external quantum efficiency of 430%, and detectivity of 9.8×10^9 Jones. These results demonstrate the efficacy of PLD as a means of mass-producing high-quality 2D ternary compounds. For the first time, Seo et al. used the PLD approach to create multi-heterojunction thin films composed of metal oxides and TMDs. Raman and TEM analyses were used to confirm the structural properties of the heterojunction thin films. They utilized thin films to construct a metal sandwich framework in order to explore the electrical properties of the multi-heterojunction TMD thin films.[110] **Table 5** summarizes the deposition conditions and characteristics of TMDs nanosheets utilizing PLD.

7. 2D Oxides Films Grown Using PLD

Recently, Jin et al. reported PLD-grown (Ga, Cu) co-doped ZnO thin films with an ultrahigh dielectric constant ($\kappa > 50$), high crystallinity, and good uniformity.[23] The κ value could also significantly tuned from 9 to 207 by carefully adjusting the concentrations of (Ga and Cu) co-dopants. Conventionally, high-performance ultrathin electronic devices require a dielectric layer with a high κ, a small amount of leakage current, and a thinner layer.[111–113] **Figure 9a** depicts how they use a typical PLD technique to produce vast-area (Ga, Cu) co-doped ZnO films with a thickness of ≈117 nm. Furthermore, using SnS_2 as a channel material, they demonstrate that the synthesized gate dielectric

Table 6. Summary of deposition conditions and properties of metal oxides nanosheets by PLD.

Year	Structure	Growth Temperature (^{0}C)	Base Pressure (Torr)	Laser Energy (J/cm^{-2})	Background Gases	Morphology	Optical/Electrical Properties	Reference
2019	ZnO/mica	600	8×10^{-6}	200 mJ 5 Hz	O_2	High-quality 2D ZnO plates in millimeter scale	Unique, self-powered UV photodetectors and UV LEDs were created	Adv. Mater. Interfaces, 2019, 6, 20, 1901156
2019	ZnO/MoS_2	650	1×10^{-3}	1	O_2	Centimeter scale thin film	type-II band alignment with a VBO of 2.52 eV and a CBO of 0.35 eV	Mater. Lett., 2019, 253, 187–190
2020	$Bi_2O_2Se/SrTiO_3$	550	8×10^{-8}	1.5	–	Wafer scale thin film of Bi_2O_2Se (22 nm)	The maximum electron mobility reaches 700 cm^{-2} V^{-1} s^{-1}@ 2K	Nanotechnology, 2020, 31, 16, 165704
2021	SnO_2/Al_2O_3 (0001)	600	1×10^{-3}	3	O_2	Large-area thin film of SnO_2	Eg = 3.95 eV	Appl. Phys. Lett., 2021, 118, 131602
2021	TiO_2/Al_2O_3 (0001)	600	1×10^{-3}	3	O_2	Large-area thin film of TiO_2	Eg = 3.30 eV	Appl. Phys. Lett., 2021, 118, 131602
2022	WO_x/Al_2O_3 (0001) $WO_x/SiO_2/Si$	500–800	3.7×10^{-7}	1.5	Ar	Large-area ultrathin flakes of WO_{3-x}	Facile conversion of PLD-grown WO_{3-x} to WS_2 films	Nanoscale, 2022, 14, 26, 9485–9497
2022	(Ga, Cu) ZnO/Al_2O_3	600	3.7×10^{-6}	300 mJ 2 Hz	–	Uniform large-area GaCuZnO films up to 5 cm.	GaCuZnO films demonstrated ultra-high κ values ranging from 9 to 207	Adv. Electron. Mater., 2022, 8, 12, 2022580
2022	$HfZrO_2$/mica	300	–	–	–	Amorphous 5 nm film of $HfZrO_2$	Ferroelectric gating	IEEE Trans. Electron. Devices, 2022, 69, 6, 3477–3482

is appropriate for 2D electronic devices (Figure 9b). The measured SnS_2-based FET device revealed a record low gate current leakage of a few hundred pA (Figure 9c), which is competitive with known dielectric materials, in addition to good repeatable and reproducible performance. The potential of 2D layered Bi_2O_2Se in state-of-the-art electronics has recently piqued the interest of the scientific community. It has been reported that the electron mobility in the new 2D layered semiconductor Bi_2O_2Se is exceptionally high (10^4 cm^2 V^{-1} s^{-1}) at 1.9 K.[114] It was recently demonstrated that CVD could be used to create high-quality 2D Bi_2O_2Se films on a variety of substrates.[115–117] On the other hand, PLD provides a practical alternative to CVD for creating highly controlled and high-quality layered 2D materials. Song et al. successfully synthesized epitaxial growth of Bi_2O_2Se films on a c-$SrTiO_3$ substrate using the PLD technique.[118] STEM and EDX mapping were used to study the nanostructure. At higher magnification (Figure 9d), an atomically precise Bi_2O_2Se-$SrTiO_3$ contact with a cross-sectional thickness of ≈23 nm can be seen. In Bi_2O_2Se, an interlayer spacing of 0.6 nm was estimated, which is compatible with its theoretical out-of-plane dimension (0.61 nm). Atomic-resolution EDX mapping makes it possible to study how Bi, O, and Se are distributed in the out-of-plane direction. The optimum electron mobility in a 70 nm thick film could reach up to 160 cm^2 V^{-1} s^{-1} at room temperature (Figure 9e). Upon cooling to 2 K, the mobility changes considerably from 160 to 700 cm^2 V^{-1} s^{-1} as depicted in Figure 9f. Li et al. presented a unique large-area growth approach (Figure 9g) that combines conventional van der Waals epitaxy (vdWE) with low-pressure PLD to overcome the vdWE bottleneck for nonlayered materials.[119] As a result, high-quality, large-area, quasi-2D ZnO single crystal flakes on various substrates were obtained using the proposed technique. This approach has also yielded ZnO film (5 nm thin) with single crystals as large as 400 µm, which is quite large among 2D ZnO single-crystal film found in the literature. Several optoelectronic devices, such as those shown in the inset of Figure 9h, have been constructed to demonstrate the use of vdWE ZnO. As demonstrated, a zero-bias responsivity spectrum typically peaks at roughly 375 nm. The response spectrum demonstrates that the detector can excellently sense UV (375 nm) and visible light (550 nm). Figure 9i depicts an *I*–*V* curve that exhibits diode-like behavior with an excellent photovoltaic effect and a UV-selective response, as well as an optoelectrical response at zero bias. They also constructed a self-powered UV photodetector and a UV LED with superior properties. Their findings demonstrate the applicability of the low-pressure PLD with vdWE method for growing quasi-2D ZnO single crystals

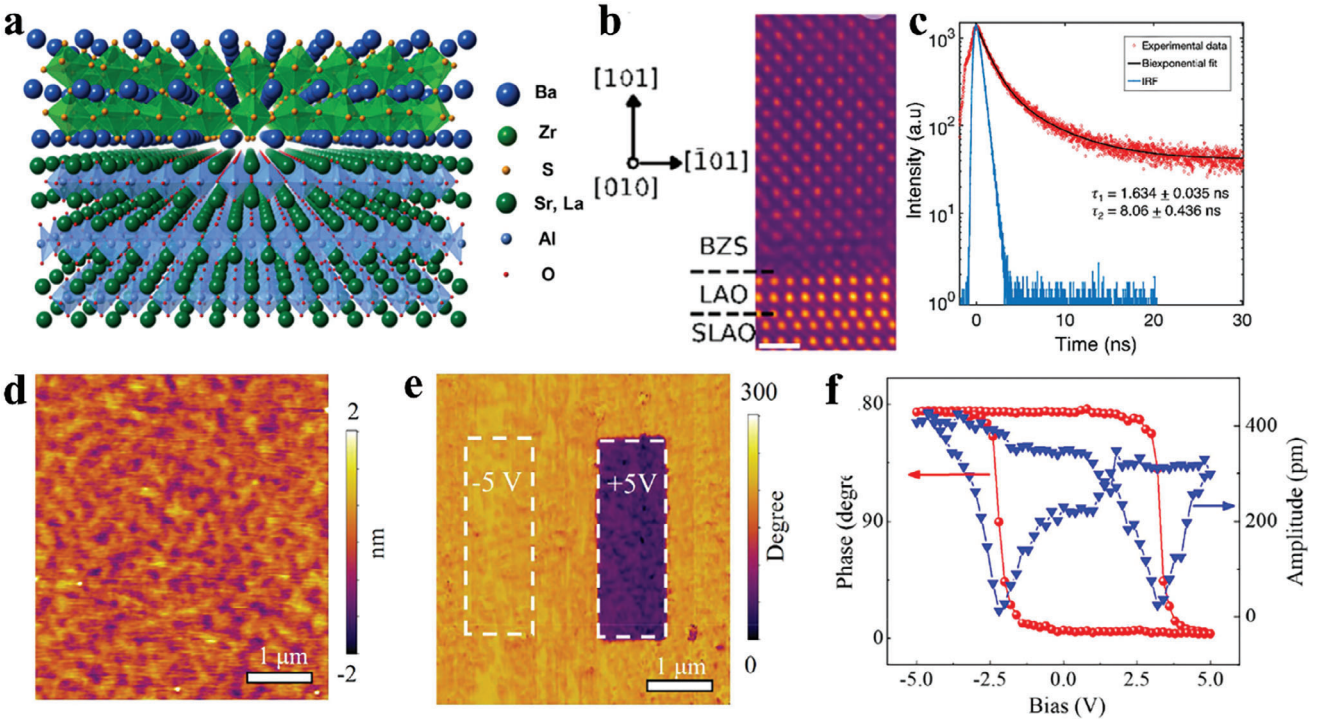

Figure 10. a) Schematic illustration of the crystal structure of the BZS/SLAO heterostructure. b) Images of the BZS/SLAO interface captured by the HAADF at atomic resolution. c) TRPL decay outline of the emission peak. d) AFM topography image of a PZT film grown on an STO substrate buffered with SRO. The epitaxial film's surface error is 0.39 nm, suggesting an excellent film. e) PFM phase picture of the film after sweeping −5 and +5 V in the areas. f) PFM amplitude and phase hysteresis curves of the PZT film. a–c) Reproduced with permission from ref. [132]. Copyright 2021, American Chemistry Society. All rights reserved. d–f) Reproduced with permission from ref. [135]. Copyright 2022, American Chemistry Society. All rights reserved.

on all layered substrates. PLD-assisted vdWE could pave the path for 2D optoelectronic device adoption in the semiconductor market.

Transparent, highly conductive metal oxides have many practical applications.[120–123] While these materials have many potential applications, more research is needed to fully understand their underlying optoelectronic features. For instance, the characterization and specification of material parameters like optical transmittance and electrical interfacial properties are crucial for improving the design and performance of these metal oxide-based devices. Thanks to the versatility of the PLD technique, Nguyen et al. studied the optical spectra of single-phase PLD-grown of ultrathin film ZnO, SnO_2, and TiO_2 transparent conducting metal oxides.[124] The 2D XRD mapping of the oxide films measured from 30° to 60° revealed prominent peaks at 2θ = 39.5°, 38.6°, and 34.4°, which could be strongly attributed to the diffraction from rutile TiO_2 (200), rutile SnO_2, and hexagonal wurtzite ZnO (0002). No secondary crystal phases were detected in the oxide film, confirming their high crystallinity. Using internal photoemission (IPE) measurements they were able to determine the zero-field barrier heights, Φ_0, as 4.31 eV for SnO_2/Al_2O_3, 4.57 eV for ZnO/Al_2O_3, and 4.61 eV for TiO_2/Al_2O_3. Work functions for these deposited metal oxides were estimated to be 6.1, 6.4, and 6.4 eV for SnO_2, ZnO, and TiO_2 with respect to the Al_2O_3 electron affinity of 1.8 eV. **Table 6** summarizes the deposition conditions and crucial features of metal oxide nanosheets formed using PLD.

8. Perovskite Thin Films Produced Using PLD

Perovskites, in particular those based on chalcogenides like layered $Ba_3Zr_2S_7$ and $BaZrS_3$, have drawn a lot of attention because of their distinctive characteristics like high absorption coefficients, prolonged recombination lifetimes, and exceptional thermal stability.[125–130] The aforementioned characteristics render them auspicious substances for employment in optoelectronics and the conversion of solar energy. Over the years, the synthesis of polycrystalline powders and single crystals, as well as theoretical methods, have significantly aided in the identification of desirable properties of chalcogenide perovskites.[129] The need to develop thin-film technology, specifically epitaxial thin films, is crucial in advancing the understanding of the physical properties of chalcogenide perovskites. Diverse groups have developed novel techniques to achieve thin films of $BaZrS_3$ through indirect methodologies. Nonetheless, the process of achieving the growth of crystalline and/or epitaxial films in a sequential layer-by-layer fashion continues to present a significant challenge. This significant procedure holds immense importance in improving our understanding of the physical characteristics of different materials, exploring the occurrence of phenomena in heterostructures, strained thin films, superlattices, and ultimately supporting various technological advancements that rely on thin-film technology, such as photovoltaics.[131] In 2021, Surendran et al. demonstrated a direct and single-step epitaxial growth of chalcogenide perovskite thin films on oxide substrates via PLD

technique.[132] The growth process was carried out at a relatively low temperature of 700 °C, and the resulting films exhibited a distinct epitaxial relationship with the substrate. Moreover, the films exhibited a band gap that is well-suited for tandem photovoltaic applications. The discovery of high-performing photodetectors is a significant breakthrough that opens up avenues for further exploration of chalcogenide perovskite heterostructures. This development also holds immense potential for advancing optoelectronic applications in the next generation. The schematic depicted in **Figure 10a** is representative of BZS films that have been grown on the $SrLaAlO_4$ (SLAO) substrate. STEM studies were conducted to examine the atomic-level quality and structure of the epitaxial BZS film that was grown on SLAO substrates. The interface between BZS and SLAO was imaged using high-angle annular dark-field (HAADF) microscopy, and the resulting atomic resolution image is presented in Figure 10b. The image confirms the epitaxial relationship between the film and substrate in this region, which is identified as (101) [001] BZS//(001) [100] SLAO. The optical properties of BZS thin films were analyzed using PL and UV-vis transmission-reflection spectroscopy. Their results indicated a band gap value of ≈1.95 eV, which was slightly higher, and a high absorption coefficient (> 10^5 cm^{-1}).[133] These characteristics make the films suitable for utilization in chalcogenide perovskite-based thin-film tandem solar cells. The findings presented in Figure 10c of this study demonstrate that the recombination times of the chalcogenide perovskites under investigation are shorter than those reported in previous studies of similar materials.[134] Further research may be required to elucidate the role of intrinsic properties and defects in influencing the recombination times of these perovskites.

Fan et al. published a report in 2022 indicating significant improvements in the ferroelectric and piezoelectric characteristics of capacitors composed of graphene/$Pb(Zr_{0.52}Ti_{0.48})O_3$/$SrRuO_3$ (GR/PZT/SRO).[135] The fabricated capacitors demonstrate superior characteristics in terms of polarization switching, switchable polarization, leakage current, and coercive voltage when compared to traditional metal-electrode ferroelectric capacitors.[136–138] The topography image of the pristine PZT/SRO film is depicted in Figure 10d, revealing a comparatively uniform surface with an average roughness of ≈0.39 nm. Subsequently, the PZT film's ferroelectric and piezoelectric characteristics are examined at the nanoscale using piezoresponse force microscopy (PFM). The PFM phase image depicted in Figure 10e was acquired subsequent to the electrical inscription of two rectangular regions with sample biases of ±5 V. In comparison to the unmarked region, the region marked with a voltage of +5 V exhibits a phase difference of 180°. The alternate region that is inscribed with a voltage of negative five volts exhibits minimal phase variation, indicating a polarizability that can be toggled to a downward orientation in its initial state of growth. The PZT film demonstrates typical ferroelectric behavior, as evidenced by a square phase loop indicating a nearly 180° switching angle and a butterfly-shaped amplitude loop observed through off-field switching spectroscopy PFM testing (Figure 10f). Overall, the study illustrated that the utilization of graphene as an electrode in PLD-synthesized PZT films leads to a considerable enhancement in ferroelectric and piezoelectric characteristics. This finding highlights the potential of graphene as a viable substitute for the development of flexible ferroelectric capacitors with superior performance. **Table 7** summarizes recent perovskite and other materials produced through PLD on various substrates (**Table 8**).

9. Other Thin Films Fabricated Using PLD

In addition to graphene, BP, h-BN, TMDCs, oxides, and perovskites, PLD is also a common technology for growing other materials. Nowadays, Bi,[139] Ge,[140] yttrium iron garnet (YIG),[141] 2D Borocarbonitrides $(BN)_{1-x}(C)_x$,[142] 10B,[143] SiC,[144] manganese porphyrin-silica hybrid films,[145] Ni_3Al-CO_3 layered double hydroxide (NiAl-LDH) film,[146] hydroxyapatite layers[147] and so on are prepared by PLD method, applied not only in electronics but also biomedical field. Among them, semimetal and YIG promising in future. With the recent development of phosphorene, interest in the elemental 2D materials of group VA (P, As, Sb, and Bi) has grown significantly. Bulk Bi is categorized as semimetal due to its small indirect band overlap of 30–40 meV. The material displays unique electronic properties when exposed to high-intensity magnetic fields. Both single-crystalline bulk and thin-film configurations of Bi demonstrate remarkably high carrier mobility at ambient temperature. These results indicate that Bi has promising prospects for utilization in logic transistors. The significant magnetoresistance effect exhibited by the Bi crystal can be explained by its notable characteristics of having a diminutive effective carrier mass and an extensive mean free path. 2D Bi films were produced using both top-down and bottom-up processes, such as liquid-based exfoliation, MBE, and acid-intercalated exfoliation. Achieving controlled synthesis of wafer-scale and high-quality atomically thin films is a prerequisite challenge for the successful integration of 2D Bi into potential applications. In a study conducted by Hao et al. in 2019, a high-quality and highly crystalline thin Bi film with atomic isolation, centimeter-scale layering, and homogeneity was successfully synthesized through the use of the PLD technique. This can be seen in **Figure 11a,b**.[139] The thin film FET device exhibits a notable carrier mobility of 220 cm^2 V^{-1} s^{-1}, as depicted in Figure 11c,d.[139] Ge is another promising semimetal material. Next, Wang et al. transferred PLD Ge/graphene heterojunction to the PI flexible substrate from copper substrate to fabricate flexible near-infrared (NIR) photodetector.[140] The Ge/Gr heterojunction exhibits dramatically improved VIS-NIR range absorption, rectification ratios of up to 13.5 at 3 V, and steady photoresponse to NIR light at zero voltage bias. Single crystal YIG thin film has been extensively researched because of the potential applications in magnonics, spintronics and related applications using magnetization dynamics owing to extremely narrow FMR linewidth as well as the low Gilbert damping coefficient, strong high magnetic properties. In 2022, Leontsev et al. researched functional properties of PLD YIG films in graphene coated Gadolinium Gallium Garnet (GGG) substrates and compared with traditional YIG on GGG.[141] YIG on graphene/GGG shows obviously higher microwave losses than YIG/GGG. This was due to the higher concentration of Fe^{2+} Cations in YIG/Graphene/GGG. Next, Jin et al. 2023 developed magneto-optical thin films of polycrystalline bilayer YIG and Ce:YIG via the PLD technique.[148] Furthermore, the MgO layer showcased in this study provides a novel solution to address heterogeneous interfaces in advanced thin

Table 7. Summary of some of recent PLD grown perovskite and other materials on various substrates.

Year	Structure	Growth Temperature (^{0}C)	Base Pressure	Laser Energy	Background Gases	Morphology	Optical/Electrical Properties	Reference
2017	$SrRuO_3/PbZr_xTi_{1-x}O_3/SrRuO_3/La_{0.7}Sr_{0.3}MnO_3/SrTiO_3$	–	–	–	–	Epitaxially grown, single crystalline, perovskite ferroelectric thin films	Effectively integrated onto a flexible platform	Adv. Mater. 2017, 29, 1605699
2017	$SrTiO_3$	720	5×10^{-6} Torr	0.6 J cm^{-2}	O_2	The $SrTiO_3$ membrane lattice collapses below a critical thickness (5 unit cells)	General relevance of interface chemical energy for the stability of quasi-2D crystalline order	Sci. Adv. 2017, 3, 5173
2017	$PbZr_{0.2}Ti_{0.8}O_3$/mica	630	100 mTorr	250 mJ	oxygen	Reliability and thermal stability	Robust operation in bent states (bending radii down to 2.5 mm) and cycling tests (1000 times)	Sci. Adv. 2017, 3, e1700121
2018	$Bi_{3.25}La_{0.75}Ti_3O_{12}$ ferroelectric films/mica or Pt	700	13 Pa	110 mJ per laser pulse	oxygen pressure	Flexible Pt/$SrRuO_3/Bi_{3.25}La_{0.75}Ti_3O_{12}$/Pt memories	Undergo 109 write erase cycles and/or 10000 times bending with 1.4 mm in radius without any fatigue or damage	ACS Appl. Mater. Interfaces, 2018, 10, 21428–21433
2019	$CeCu_3Mn_4O_{12}/YAlO_3$(110)	740–790	40 Pa	1.1 J cm^{-2}	O^{2+} 5–10% O_3	$CeCu_3Mn_4O_{12}$ epitaxial thin film grown on $YAlO_3$(110)	A Neel temperature exceeding 400 K and metallic transport properties at room temperature, uniaxial magnetic anisotropy	ACS Appl. Electron. Mater. 2019, 1, 2514–2521
2019	$CsPbBr_3$	320	10^{-3} Pa	100 mJ	–	$CsPbBr_3$ thin film displays good stability in a high-humidity environment	Achieve the highest power conversion efficiency of 6.3%	ACS Appl. Energy Mater. 2019, 2, 2305–2312
2019	$Ba_{0.67}Sr_{0.33}TiO_3$	680	15 Pa	90 mJ	O_2	Excellent dielectricity. mechanical flexibility and durability	Excellent Dielectric Properties over a Wide Range of Frequencies (dielectric constant more than 1200)	ACS Appl. Mater. Interfaces, 2019, 11, 27088–27097
2021	$Cs_2AgBiBr_6$	200	1.5×10^{-1} mbar	0.45 J cm^{-2}	Ar gas	Obtain high-quality $Cs_2AgBiBr_6$ films with grain sizes > 200 nm	Direct band gap of 2.24 eV, PL centered at 1.90 eV	Chem. Mater. 2021, 33, 7417–7422
2021	$CsCu_2I_3$	100	1×10^{-4} Pa	–	–	The thin film quality and optoelectronic properties improved	The peak responsivity and specific detectivity of the detector are 49.22 mA W^{-1} and 2.49×10^{12} cm Hz$^{1/2}$ W^{-1}	Adv. Optical Mater. 2021, 9, 2100889

(*Continued*)

Table 7. (Continued)

Year	Structure	Growth Temperature (^{0}C)	Base Pressure	Laser Energy	Background Gases	Morphology	Optical/Electrical Properties	Reference
2021	$PbZr_{0.2}Ti_{0.8}O_3$	600	13 Pa	1.3 to 7.6 J cm^{-2}	oxygen pressure	Achieve highly strained phases with large tetragonal distortions in Pb-based ferroelectric films	Large Poisson's ratio and negative thermal expansion	Adv. Sci. 2021, 8, 2003582
2022	$CsPbBr_3$	–	–	1.93 µm	–	Patterned perovskite films with high quality, submicron precision, and well-defined edges	LEDs exhibit good emission characteristics	ACS Appl. Mater. Interfaces, 2022, 14, 46958–46963
2022	(La, Lu, Y, Gd, Ce)Al_2O_3	775	4.5×10^{-7} Torr	2.00 J cm^{-2}	oxygen pressure of 1.1 Torr	The synthesis of a highly epitaxial thin film of configurationally disordered rare-earth aluminum perovskite oxide	The potential for high-energy conversion	Adv. Sci. 2022, 9, 2202671
2022	Ba_2BiMO_6 (M = Bi, Nb, Ta)	550	1 Pa	1.0 J cm^{-2}	oxygen partial pressure	High-quality Ba_2BiMO_6 epitaxial thin films	The fabrication of Ba_2BiTaO_6 – Nb doped $SrTiO_3$ P–N junction diodes	Adv. Sci. 2022, 9, 2104141
2022	$BaTiO_3$ (BTO)	650	2×10^{-6} mbar	1 J cm^{-2}	annealed at 550°C in an oxygen pressure of 300 mbar for 1 h	The strong piezoelectric performance of the free-standing complex oxide $BaTiO_3$ (BTO)	Create ultrathin piezoelectric resonators demonstrated that the device can be brought into mechanical resonance by piezoelectric actuation	Adv. Mater. 2022, 34, 2204630
2022	$SrRuO_3$ (SRO)	670	20 Pa	1.1 J cm^{-2}	oxygen	SRO buffer layer acting as the bottom electrode	The GR/PZT/SRO capacitors exhibit more abrupt polarization switching, larger switchable polarization, lower leakage current, and smaller coercive voltage	ACS Appl. Mater. Interfaces 2022, 14, 17987 – 17994
2023	$CaRuO_3$ and $SrTiO_3$	670	40 Pa	1.2 J cm^{-2}	oxygen pressure	Constructing superlattices using PLD $CaRuO_3$ and $SrTiO_3$	A symmetry-mismatch-driven interfacial phase transition from paramagnetic to ferromagnetic state	Adv. Funct. Mater. 2023, 2300338

(*Continued*)

Table 7. (Continued)

Year	Structure	Growth Temperature (^{0}C)	Base Pressure	Laser Energy	Background Gases	Morphology	Optical/Electrical Properties	Reference
2023	$SrTiO_3$ (STO)	700	1×10^{-7} mbar	2 J cm^{-2}	–	Grow a high-quality STO pseudo substrate	For further overgrowth of functional oxides, such as $PbZr_{1-x}Ti_xO_3$ (PZT)	ACS Appl. Mater. Interfaces 2023, 15, 6058–6068
2019	Bi/SiO_2 (300 nm)/Si or sapphire substrates	100 °C and RT	3×10^{-5} Pa	300 mJ	–	Centimeter scale-Bi thin films	p-type transistor, the extracted carrier mobility is $\approx 220\,cm^{-2}\,V^{-1}\,s^{-1}$	InfoMat. 2019, 1, 98–107
2023	Ce:YIG	650	10 mTorr	2.5 J cm^{-2}	oxygen partial pressure	The nucleation and growth of a nanocrystalline garnet structure in YIG/Ce:YIG with promoted phase purity, density, and crystallinity	Give rise to improved magnetic, optical and magneto-optical properties in YIG/Ce:YIG	ACS Materials Lett. 2023, 5, 803–810

film devices by serving as both a diffusion barrier and a structure template. The PLD technique fabricates an MgO interfacial layer on the Si (100) substrate. Subsequently, the YIG and Ce:YIG layers are deposited atop, with YIG serving as the initial layer for Ce:YIG as the seed layer. As Figure 11e,f shows, their study aimed to attain a superior level of phase purity and enhanced crystallization, aiming to produce a structure consisting of Si/ZnO/YIG/Ce:YIG. The alterations made to the chemistry and microstructure of YIG/Ce:YIG has led to enhancements in its magneto-optical characteristics. Specifically, there has been a 38% rise in Faraday rotation, a 15% increase in saturation magnetization, and a 20% increase in IR transmission. Except semimetal and YIG thin films, 2D Borocarbonitrides $(BN)_{1-x}(C)_x$, 10B, SiC, manganese porphyrin-silica hybrid films, $Ni_3Al\text{-}CO_3$ layered double hydroxide (NiAl-LDH) film, hydroxyapatite layers and so on are prepared by PLD method. And these materials are applied in more fields, which expand the usage of PLD technology.

10. Heterojunction Thin Films Fabricated Using PLD

PLD is a powerful technique for fabricating large-scale 2D heterojunction thin films, renowned for its high stoichiometric fidelity and simple process control. This technology drives innovative developments in designing and fabricating various heterostructures, including topological insulators, layered semiconductors, graphene, and van der Waals materials.[30,149,150] These heterojunctions exhibit diverse properties suitable for applications in nanoelectronics, photovoltaics, thermoelectrics, and photonics, offering unmatched opportunities in material science and device engineering.[151-153] The unique band engineering of these heterostructures improves device performance by controlling carrier mobility, modulating bandgaps, enhancing light absorption, and managing thermal transport properties.[154,155] The versatility of PLD allows for the combination of different materials in a single heterostructure, paving the way for devices with novel properties and functionalities that would be impossible to achieve using conventional semiconductor technologies. In 2021, Seo et al. demonstrated the successful fabrication of centimeter-scale thin films of multiheterojunction TMDCs on a silicon-based substrate using a sequential PLD technique.[110] Also, in order to test the electrical characteristics of their heterostructure thin films for potential use in electronic devices, they constructed a metal sandwich structure based on PLD-grown heterostructure, which suggested decent capabilities. Zakto et al. (2023) presented an approach to derive functional van der Waals stacks of 2D semiconductors using PLD technique. Switching targets allows a $WS_2/WSe_2/WS_2$ heterostructure to be fabricated in situ.[154] The PLD concept for heterostructure synthesis is shown in **Figure 12a**. Raman spectroscopy probes the crystallization of WS_2 and WSe_2, and structural and chemical analyses demonstrate a well-defined heterostructure. The major WSe_2 (top layer) Raman peak disappears after many months (8) of ambient exposure. However, as a comparison, they show the same time-dependent study of the van der Waals heterostructure with a buried WSe_2 layer. This observation suggests that the WSe_2 layer remained shielded during the in situ formation of the heterostructure, thereby preventing any potentially detrimental reactions with the ambient atmosphere (Figure 12b). Subsequently they also demonstrated that PLD growth of van der Waals heterostructures has the potential for direct integration into functional devices. The devices are then measured at 4 K in an AC + DC cryogenic configuration, revealing a high resistivity and conductance maxima at ≈300 mV (Figure 12c). This verifies the well-type energy band-gap obtained by arranging various 2D semiconductors, which enables the customization of charge transport properties.

In 2023, D'Agosta et al. used PLD in an ultra-high vacuum to fabricate WS_2/MoS_2 and the reverse heterostructure MoS_2/WS_2

Table 8. Summary of some of recent PLD grown heterostructures on various substrates.

Year	Structure	Growth Temperature	Base Pressure	Laser Energy	Background Gases	Morphology	Optical/Electrical Properties	Reference
2021	$BiFeO_3$/La2/3Sr1/3MnO_3	800/950 °C	100/200 mTorr	60/70 mJ	O_2	The complex magnetic interactions at the interface	A sizable exchange bias (HEB≈30 Oe at 10 K) in the magnetic hysteresis	Phys. Rev., B Condens. Matter, 2022, 639, 15, 414023
2021	$WS_2/WSe_2/WS_2$	400 °C	10^{-8} mbar	80 mJ	0.1 mbar of Ar	Large scale, the structural preservation of encapsulation	a vertical tunneling device	ACS Nano 2021, 15, 4, 7279–7289
2022	$Sr_3Al_2O_6$/MgO	750/700 °C	2×10^{-8} torr	0.7/1.7 J cm^{-2}	2×10^{-6} torr O_2 pressure	a lift-off and transfer method	3D racetracks from freestanding magnetic heterostructures grown on a water-soluble sacrificial release layer	Nat. Nanotechnol. 2022, 17, 1065–1071
2022	FeSe/Sb_2Te_3/FeSe	700/900 °C	–	–	–	high-quality freestanding multiferroic heterostructures	a strong strain gating effect with bending and a sharp FMR shift	Nanoscale, 2022, 14, 10889–10902
2022	$ZrTe_2/SrTiO_3$	550/170 °C	5×10^{-5} Pa	–	–	enhanced thermoelectric performance induced by interfacial effect	large thermoelectric power factor, large Seebeck coefficient and high electrical conductivity	J. Materiomics 2022, 8, 3, 570–576
2022	pentacene/MoS_2	428 K	–	2 J cm^{-2}	–	the formation of atomically thin pentacene/MoS_2 lateral heterostructures	The density of states changes sharply across the pentacene/MoS_2 interface	J. Phys. Chem. C 2022, 126, 1132–1139
2022	25%-Fe-doped Cu_2ZnSnS_4 (CZFTS)/Bi_2S_3	750 °C	18 MPa	–	Ar	combining partial cation substitution and in situ PLD technique	at least one order of-magnitude improvement in photoelectric response speed within visible light (Vis) region, and responding time is decreased to a few milliseconds	J. Alloys Compd. 2022, 906, 164359
2022	$SrTiO_3/SrRuO_3$	680/700 °C	2.66/13.33 Pa	–	Oxygen	the restriction of oxygen vacancy migration through the SRO-rich interface layer formed on the $SrRuO_3$ surface	improves the retention time of the device	Sci. China Mater. 2023, 66, 3, 1140–1147
2023	MoS_2–WS_2	–	10^{-10} mbar	2 J cm^{-2}	–	high coverage and thickness sensitivity	the interlayer coupling is not substrate-dependent	Nanoscale, 2023, 15, 7493–7501
2023	$Pr_{0.6}Sr_{0.4}MnO_3$/$Pr_{0.5}Ca_{0.5}MnO_3$	–	–	–	–	phase-segregated nature	the kinetic arrest and training effect	Sci. Rep. 2023, 13, 2315

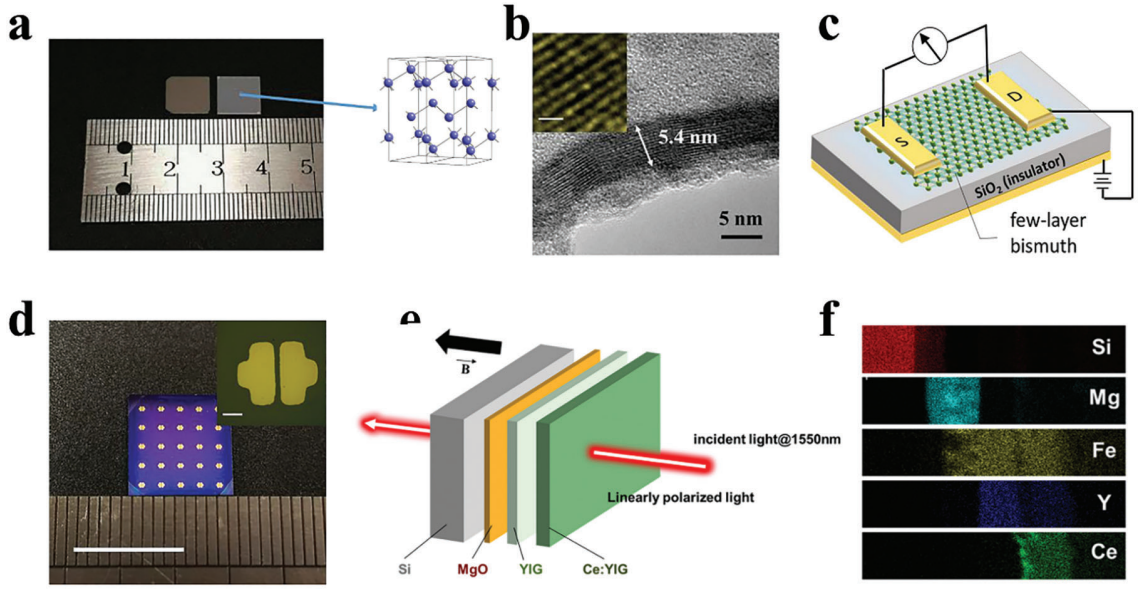

Figure 11. a) (Left) Optical photographs of thin Bi film samples grown on different substrates (left: SiO_2 (300 nm)/Si, right: Al_2O_3) by PLD. (Right) The schematic of crystal structure of bulk bismuth. b) Cross-sectional TEM image of the 5.4-nm-thick Bi film. The inset image shows the enlarged cross-sectional TEM image, demonstrating well-defined layered structure (scale bar = 1 nm). c) The schematic of FETs based on Bi film. d) Photograph of Bi FETs with patterned Au electrode (scale bar = 1 cm). The inset shows the optical picture of the electrode pattern of the device (scale bar = 100 μm). e) Schematic diagram of the garnet bilayer of YIG/Ce:YIG integrated onto silicon with an MgO interfacial layer. f) EDS elemental mapping for Si, Mg, Fe, Y, and Ce. a–d) Reproduced with permission from ref. [139]. Copyright 2019, WILEY-VCH Verlag GmbH & Co. KGaA. All rights reserved. e,f) Reproduced with permission from ref. [148]. Copyright 2023, American Chemistry Society. All rights reserved.

on Au (111).[156] As depicted in Figure 12d, this experimental method allowed them to investigate the heterostructure growth in situ and analyze its morphology and nanoscale structure using scanning tunneling microscopy (STM). After the second and third cycles, the WS_2 islands that had developed at random on the MoS_2/Au surface had grown in size. In the first two cycles, the density of the islands rose, and the WS_2 area grew linearly with the number of laser pulses, as seen in Figure 12e. As shown summarized in Figure 12f, the area of WS_2 exhibits a linear growth pattern in response to laser pulses, wherein the density of islands initially increases during the first two cycles but subsequently decreases due to coalescence. The emergence of second-layer WS_2 islands becomes evident once the coverage reaches 0.9 ML, suggesting that the growth of heterobilayers adheres to a layer-by-layer mechanism. The process of addressing voids resulting from the merging of nanoislands necessitates the application of a significant proportion of second-layer WS_2 deposition. PLD-grown heterobilayers on silica support were successfully transferred, elucidating their relationship with the vibrational characteristics of the Au substrate. To better understand the vibrational effects associated with the interface with the growth substrate and coupling between TMD layers, this investigation delves into the PLD technique's capacity to manufacture TMD heterobilayers with good coverage and thickness control.

Park et al. (2023) additionally explored the PLD-mediated growth of centimeter-scale 2D WSe_2/Bi_2O_2Se thin films.[152] Initially, they deposited Bi_2O_2Se and WSe_2 multilayers on a c-cut sapphire substrate using directly in situ PLD. As depicted in Figure 12g, they investigate the structural, electrical, and optical properties of the WSe_2/Bi_2O_2Se heterostructure. The photoresponse characteristics of the WSe_2/Bi_2O_2Se heterostructure were evaluated using normalized time-dependent photoresponse under simulated chopped irradiation with a 20 s on/off interval with multiple cycle replay. As a result, ≈110% of the on/off photoresponse ratio was observed. Figure 12h demonstrates that multilayer Bi_2O_2Se thin films have a lower photoresponse than heterostructures. The enhanced photoresponse features of the heterostructure are attributable to its type-II band alignment, which facilitated the charge transfer of photogenerated carriers from the heterostructure.

Sha et al. (2022) conducted the synthesis of thin films of $Cu_2Zn_{0.75}Fe_{0.25}SnS_4$ (CZFTS) with a 25% iron doping by partially substituting zinc.[157] Additionally, they incorporated the electron acceptor Bi_2S_3 into CZFTS, resulting in the formation of a CZFTS/Bi_2S_3 heterostructure. The combination of partial cation substitution and in-situ PLD techniques shows promise in the development of visible-active CZTS-based thin-film photodetectors (Figure 12i). This approach offers an effective and efficient method for producing economically viable thin-film photoelectric devices based on plenary chalcogenide compounds. Tumino et al. (2022) examined a hybrid heterostructure involving pentacene molecules and 2D MoS_2 crystals.[158] The heterostructure was fabricated on Au(111) substrate using a combination of PLD and organic molecular beam epitaxy techniques. The structures were examined in situ using STM, which effectively demonstrated the development of atomically thin pentacene/MoS_2 lateral heterostructures. The

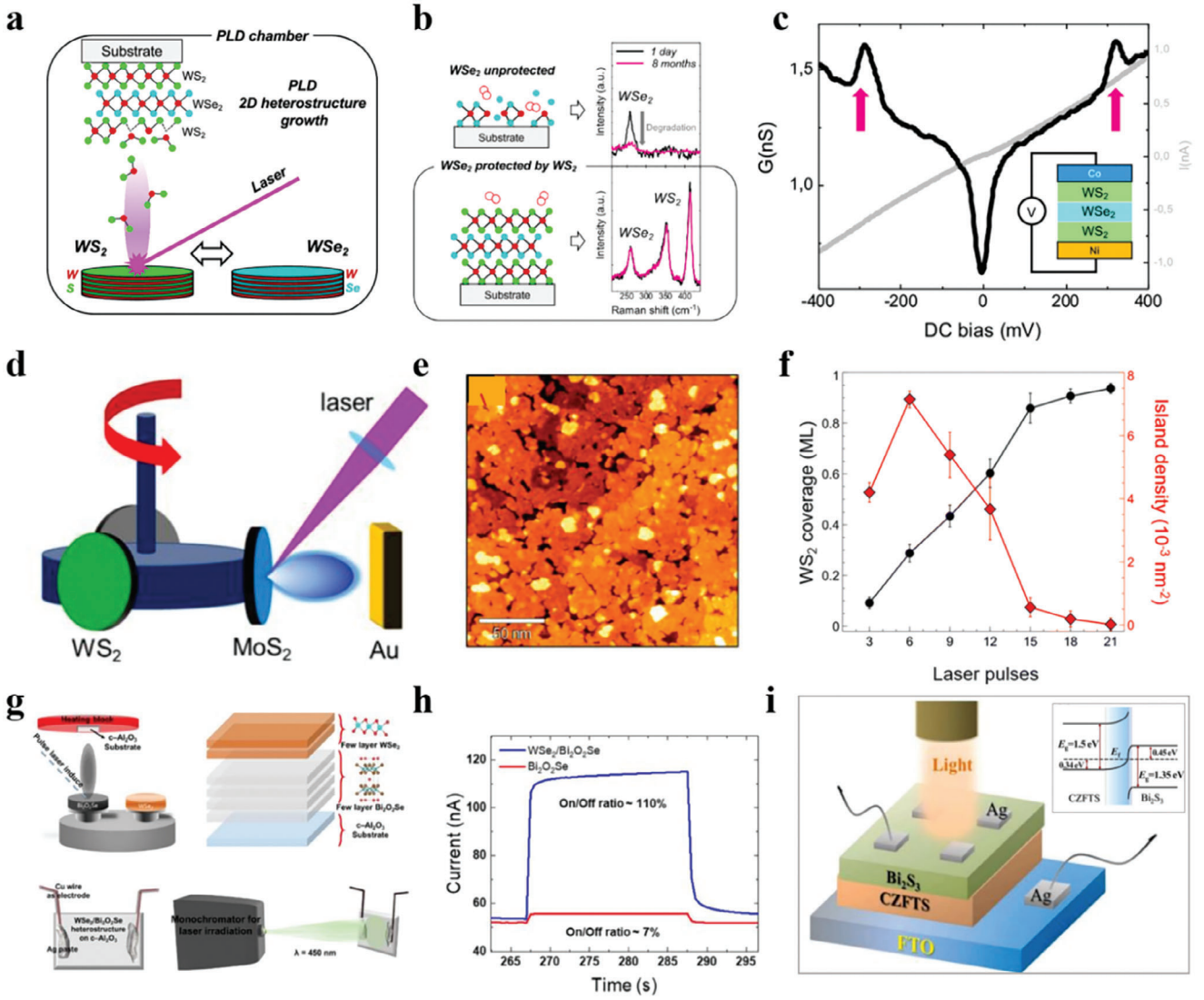

Figure 12. a) 2D heterostructure PLD growth technique entails ablating stoichiometric targets of TMDC 2D semiconductors with a Nd:YAG laser in a 10^{-1} mbar high-purity Ar atmosphere. This approach facilitates the direct integration of 2D materials into van der Waals heterostructures by facilitating layering via in situ target modification. b) WSe_2 heterostructure evolution after ambiance exposure, with Raman spectra recorded on WSe_2 and WS_2/WSe_2/ WS_2 samples. WSe_2 deteriorates (after 8 months) without protection, while embedded in WS_2 layers maintains unaffected Raman spectra. c) Transport measurements in vdW 2D semiconductor heterostructures reveal symmetric resonances at ±300 mV, emanating from the engineered quantum well energetic topography. d) Schematic illustration of the PLD setup, in which targets are affixed on a rotating carousel that enables selection of the deposition material. e) Wide-range STM images of WS_2 on MoS_2/Au(111). f) Area of WS_2 and island density as a function of laser pulse count. g) Schematic of WSe_2/Bi_2O_2Se device fabrication, deposition, stacking, wiring, and photoresponse measurement using a monochromator. h) Time-dependent photoresponses of Bi_2O_2Se (red) and WSe_2/Bi_2O_2Se (blue) heterostructures the bias of 0.1 V and the illumination of 450 nm. i) A diagram depicting a typical photoelectric response testing system. The alignment of the energy bands in a state of thermodynamic equilibrium is shown inset. a–c) Reproduced with permission from ref. [154]. Copyright 2021, American Chemistry Society. All rights reserved. d–f) Reproduced with permission from ref. [156]. Copyright 2023, Royal Society of Chemistry. All rights reserved. g,h) Reproduced with permission from ref. [152]. Copyright 2023, American Chemistry Society. All rights reserved. i) Reproduced with permission from ref. [157]. Copyright 2018, Elsevier. All rights reserved.

density of states exhibits a pronounced variation at the interface between pentacene and MoS_2, suggesting a limited interfacial coupling that does not significantly affect the electronic characteristics of MoS_2 edge states. Their research reveals the self-organization phenomenon in abrupt mixed-dimensional lateral heterostructures. This discovery has significant implications for developing hybrid devices that rely on organic/inorganic 1D junctions.

11. Theoretical Analysis During PLD Process

For the theoretical analysis during PLD process, it mainly focuses on investigating the influence of growth conditions on material quality through MD simulation and DFT calculation, which could help us to get the high-quality thin films or heterojunctions, and to develop a better understanding on material growth process.

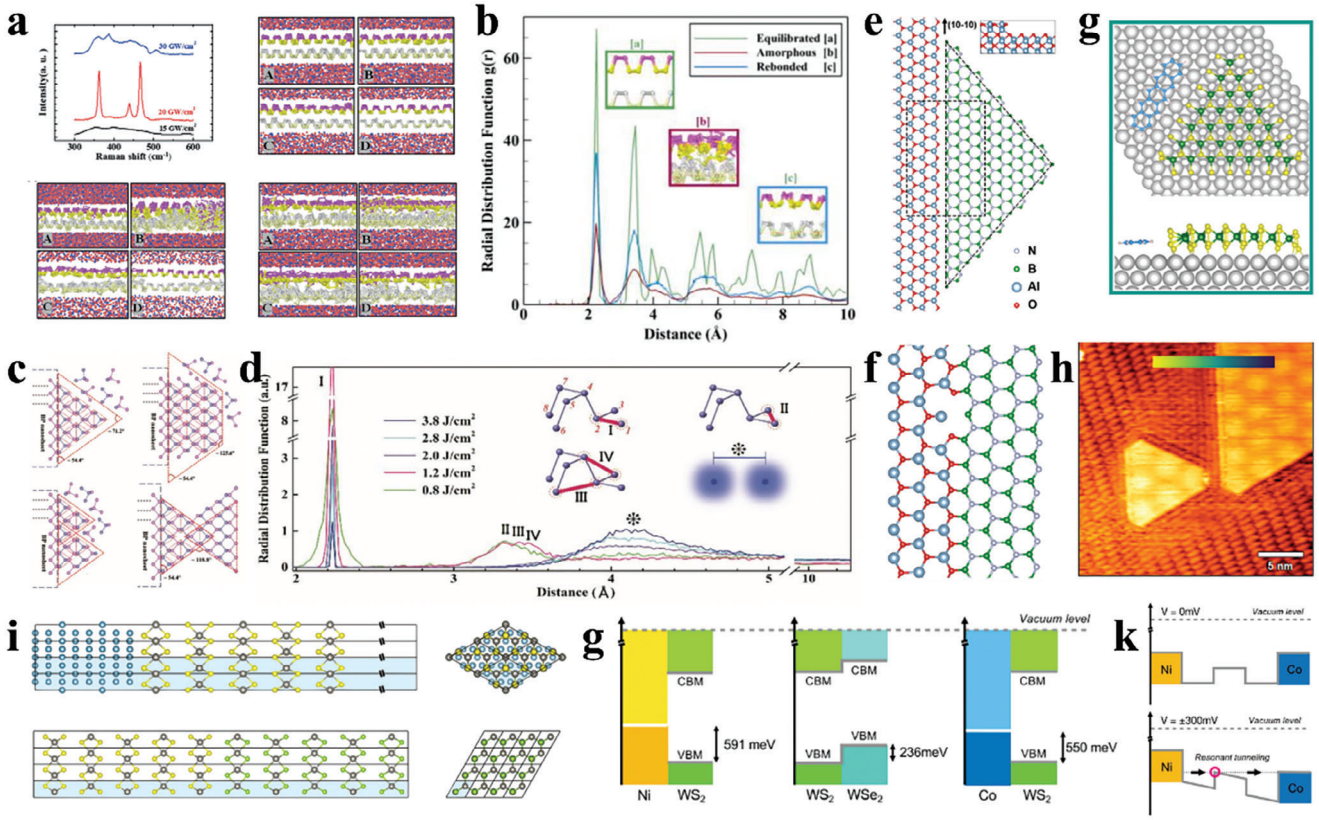

Figure 13. a) Impact of laser energy on BP thin films. b) Radial distribution function (RDF) plots illustrating three stages of metaphase transformation at 20 GW cm^{-2}. c) Schematic representation of domain formation and sheet merging during lateral growth of BP. Pink and purple balls represent upper/lower-group atoms in mono/bilayer BP respectively. d) MD simulation on laser fluence effect during PLD process. RDF curves from MD simulation with different laser fluence. Four characteristic peaks (I-IV) identify BP allotrope fingerprints, distinguishing between phosphorus allotropes. e) Schematics of zigzag h-BN/c-Al_2O_3 interface. Top view illustration of the interface between O-terminated sapphire step-edge (along (10–10) direction) and B-terminated ZZ h-BN edge. The inset shows the side view of the step-edge configuration in the substrate, with a dashed triangle denoting the seed of the triangular domain observed in experiments. f) Relaxed structure of the dashed rectangle in(a). The defect involves the displacement of oxygen atoms from the plane toward the second Al_2O_3 layer, while maintaining a bond with the adjacent boron atom. Only the topmost layer's Al/O atoms are displayed here for clarity. g) Top and side perspectives of the DFT structures representing pentacene adsorption at the border between MoS_2−S100 and Au (parallel orientation). h) STM image of pentacene/MoS_2 on Au(111) showing the interfacial regions of the lateral heterostructure (0.8 V, 0.15 nA) i) Ball-and-stick representation of two lattice-matched interfaces used to estimate natural band offsets in the functional van der Waals device. j) Energy profiles across the device schematized. Computed band offsets at different interfaces of the contacted van der Waals heterostructure. k) The computed band offsets are represented by vertical bars. a,b) Reproduced with permission from ref. [84]. Copyright 2018, WILEY-VCH Verlag GmbH & Co. KGaA. All rights reserved. c,d) Reproduced with permission from ref. [15]. Copyright 2021, Nature Portfolio. All rights reserved. e,f) Reproduced with permission from ref. [71]. Copyright 2022, Elsevier BV. All rights reserved. g,h) Reproduced with permission from ref. [158]. Copyright 2023, American Chemical Society. All rights reserved. i–k) Reproduced with permission from ref. [154]. Copyright 2021, American Chemical Society. All rights reserved.

In 2018, Qiu et al. conducted MD simulations to investigate the physical mechanism behind confined laser-induced metaphase transformation (**Figure 13a**).[84] The ultrafast laser ablation of the BP layer under confinement generates transient non-equilibrium conditions characterized by high temperature and pressure, lasting for a few picoseconds. By optimizing the laser intensity, this process initiates a metaphase transformation, resulting in the formation of a crystalline BP thin film on the substrate. The MD simulations have provided further evidence of the metaphase transformation process. The recrystallization process of amorphous phosphorus to black phosphorus can be derived from the three radial distribution function curves as shown in Figure 13b. Wu et al. directly synthesized few-layered BP on a centimeter scale with high crystallinity and homogeneity by PLD and developed a theoretical insight on the atomic structural evolution under laser heating from MD simulations (Figure 13c,d).[15] The utilization of pulsed laser with appropriate energy-induced ablation leads to the activation of plasma region, which promotes the formation of large-scale BP clusters in physical vapor, thereby reducing the formation energy of BP phase and enabling the growth of few-layer BP. Figure 13c vividly illustrates the layer growth and sheet merging process of monolayer BP, which includes the formation of domains and the merging of sheets. This process is facilitated by the advantageous zigzag edge and the connection of phosphorus clusters. The resulting BP sheets exhibit isosceles triangles or trapezoidal domain shapes, which eventually merge into a large-area film on the substrate. Pulsed laser has also been reported to be utilized for the growth of layered graphene, by adjusting the laser energy density to endow the incident carbon atoms with sufficient kinetic energy,

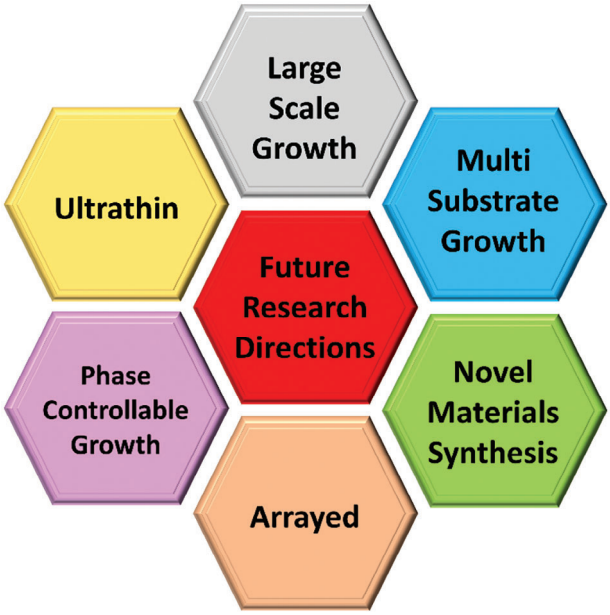

Figure 14. An original figure outlining the future research direction of PLD technique.

enabling them to overcome the energy barrier and undergo sustained diffusion within the layers, leading to the formation of 2D islands.[51]

Using DFT calculations, Biswas et al. investigated the underlying mechanism of unidirectional domain growth induced by PLD. A significantly wide bandgap h-BN thin film with pronounced unidirectional triangular domain morphology was directly grown on an insulating planar sapphire substrate using PLD (Figure 13e).[71] This unidirectional domain growth is attributed to the step-edge guided nucleation caused by reducing the symmetry and energy of the film-substrate interface, thereby breaking the degeneracy of nucleation sites for random domain formation. It is observed through simulation that there is a significant energy preference for the specific formation of unidirectional domains of h-BN on Al_2O_3. This energy preference ensures the dominance of a single interface configuration, ultimately resulting in the growth of h-BN in a unidirectional manner. Additionally, the lower lattice mismatch leads to the spontaneous formation of subgrain boundary dislocations (Figure 13f).

Tumino et al. simulated the formation mechanism of pentacene/MoS_2 lateral heterostructures grown via PLD and organic molecular beam epitaxy using DFT.[158] By analyzing the adsorption energies, geometric orientations, and interfacial interactions, it was found that pentacene and MoS_2 are most favorable for forming lateral heterostructures. The theoretical models and STM images of the pentacene/MoS_2 lateral heterostructure on Au(111) are depicted in Figure 13g,h, respectively. The natural band offsets at the lattice-matched interface between WS_2 and WSe_2 (Figure 13i) were calculated, revealing the staggered gap at the WS_2/WSe_2 interface, which results in the formation of a quantum well in the functional device.[154] Additionally, the relative positions of the Ni and Co electrodes with respect to the WS_2 valence band maximum (VBM) were determined, confirming the observed symmetric transport behavior in the experiment (Figure 13j). The resonance mechanism responsible for the transport characteristics is illustrated in Figure 13k. These findings provide evidence for the existence of a quantum well achieved through resonant transport.

12. Summary and Prospective

In order to achieve the extensive utilization of highly integrated 2D devices, it is imperative to have large-sized thin films that can ensure optimal material quality and uniformity of properties. Currently, the task of scaling up the growth of all 2D thin films to the wafer level remains a significant challenge. This review provides a comprehensive overview of the latest developments in the preparation of 2D films using PLD. The discussion encompasses growth mechanisms, strategies, and materials classification. At first, we highlight the efficient approaches to developing PLD techniques. Subsequently, the growth, characterization, and device applications of diverse 2D films are expounded upon, including but not limited to graphene, h-BN, MoS_2, BP, oxides, perovskite, and semi-metal. Ultimately, the challenges in these fields are presented, and additional research underscores the significance of the PLD methodology.

PLD exhibits several characteristics that render it highly appealing for the growth of films of intricate materials. The aforementioned factors encompass the stoichiometric transference of matter from the target, production of high-energy species, the hyperthermal interaction between the ablated cations and ambient gas in the ablation plasma, and adaptability to background pressures that span from ultrahigh vacuum to 1 Torr. The deposition of multination films can be accomplished through the utilization of either singular, stoichiometric targets of the material of interest or through the use of multiple targets for each element when employing PLD. The thickness distribution resulting from a stationary plume in PLD exhibits significant non-uniformity owing to the highly forward-directed nature of the ablation plume. Nevertheless, certain obstacles have been encountered by PLD techniques. Initially, it is noteworthy that the caliber of films produced through the PLD method is comparatively inferior to those generated through ALD and MBE techniques. Consequently, researchers must address certain deficiencies of the PLD approach, including but not limited to thickness inhomogeneity, restricted scale, and inadequate continuity. Furthermore, the range of PLD-grown materials that have been investigated is considerably restricted in comparison to the extensive array of materials within this particular family. In addition, the researchers may consider exploring alternative doping techniques for material synthesis involving varying elements and concentrations. Doping engineering has the potential to alter the structures and properties of materials in comparison to their pure counterparts. Ultimately, a comprehensive investigation was conducted into the essential mechanisms underlying 2D and thin film production via PLD. Currently, thin films have exhibited significant potential for fundamental research and fabrication of a diverse array of electronic and optoelectronic devices. Historically, it has been demonstrated that PLD is capable of facilitating the growth of single-layer thin film and heterostructures by manipulating various targets without compromising the vacuum. As **Figure 14** shows, regarding the future development direction of PLD technology, ultra-thin large-area high-quality films or arrays are produced on

different substrates, with new structures or new material types. The notion that PLD will assume a significant function in the fabrication of materials and devices is widely held.

Acknowledgements

This work was supported by the National Key Research and Development Program of China (2022YFB3807200), National Natural Science Foundation of China (52222101), Key-Area Research and Development Program of Guangdong Province (No.2020B010170002) and the Innovation and Technology Fund, HKSAR (No. ITS/215/20FP).

Conflict of Interest

The authors declare no conflict of interest.

Keywords

2D films, device application, electronics, large-scale synthesis, pulsed laser deposition

Received: September 21, 2023
Revised: November 22, 2023
Published online: December 12, 2023

[1] F. Chen, Q. Tang, T. Ma, B. Zhu, L. Wang, C. He, X. Luo, S. Cao, L. Ma, C. Cheng, *InfoMat.* **2022**, *4*, e12299.
[2] S. Das, A. Sebastian, E. Pop, C. J. McClellan, A. D. Franklin, T. Grasser, T. Knobloch, Y. Illarionov, A. V. Penumatcha, J. Appenzeller, Z. Chen, W. Zhu, I. Asselberghs, L.-J. Li, U. E. Avci, N. Bhat, T. D. Anthopoulos, R. Singh, *Nat. Electron.* **2021**, *4*, 786.
[3] T. Knobloch, Y. Y. Illarionov, F. Ducry, C. Schleich, S. Wachter, K. Watanabe, T. Taniguchi, T. Mueller, M. Waltl, M. Lanza, M. I. Vexler, M. Luisier, T. Grasser, *Nat. Electron.* **2021**, *4*, 98.
[4] L. Ma, R. Chen, S. Dong, T. Yu, *InfoMat.* **2022**, *4*, e12310.
[5] Y. Ma, Y. Cheng, J. Wang, S. Fu, M. Zhou, Y. Yang, *InfoMat.* **2022**, *4*, e12328.
[6] F. Wu, H. Tian, Y. Shen, Z. Hou, J. Ren, G. Gou, Y. Sun, Y. Yang, T. L. Ren, *Nature* **2022**, *603*, 259.
[7] F. Xia, H. Wang, J. C. M. Hwang, A. H. C. Neto, L. Yang, *Nat. Rev. Phys.* **2019**, *1*, 306.
[8] K. Zhu, C. Wen, A. A. Aljarb, F. Xue, X. Xu, V. Tung, X. Zhang, H. N. Alshareef, M. Lanza, *Nat. Electron.* **2021**, *4*, 775.
[9] D. Jayachandran, A. Oberoi, A. Sebastian, T. H. Choudhury, B. Shankar, J. M. Redwing, S. Das, *Nat. Electron.* **2020**, *3*, 646.
[10] N. Li, Q. Wang, C. Shen, Z. Wei, H. Yu, J. Zhao, X. Lu, G. Wang, C. He, L. Xie, J. Zhu, L. Du, R. Yang, D. Shi, G. Zhang, *Nat. Electron.* **2020**, *3*, 711.
[11] Y. Cao, S. Chen, Q. Luo, H. Yan, Y. Lin, W. Liu, L. Cao, J. Lu, J. Yang, T. Yao, S. Wei, *Angew. Chem. Int. Ed. Engl.* **2017**, *56*, 12191.
[12] Y. Y. Illarionov, A. G. Banshchikov, D. K. Polyushkin, S. Wachter, T. Knobloch, M. Thesberg, L. Mennel, M. Paur, M. Stöger-Pollach, A. Steiger-Thirsfeld, M. I. Vexler, M. Waltl, N. S. Sokolov, T. Mueller, T. Grasser, *Nat. Electron.* **2019**, *2*, 230.
[13] A. J. Yang, K. Han, K. Huang, C. Ye, W. Wen, R. Zhu, R. Zhu, J. Xu, T. Yu, P. Gao, Q. Xiong, X. Renshaw Wang, *Nat. Electron.* **2022**, *5*, 233.
[14] S. Parmar, N. Prajesh, M. Wable, R. J. Choudhary, S. Gosavi, R. Boomishankar, S. Ogale, *iScience* **2022**, *25*, 103898.
[15] Z. Wu, Y. Lyu, Y. Zhang, R. Ding, B. Zheng, Z. Yang, S. P. Lau, X. H. Chen, J. Hao, *Nat. Mater.* **2021**, *20*, 1203.
[16] Z. Yang, J. Hao, S. Yuan, S. Lin, H. M. Yau, J. Dai, S. P. Lau, *Adv. Mater.* **2015**, *27*, 3748.
[17] Z. Yang, W. Jie, C. H. Mak, S. Lin, H. Lin, X. Yang, F. Yan, S. P. Lau, J. Hao, *ACS Nano* **2017**, *11*, 4225.
[18] A. K. Geim, I. V. Grigorieva, *Nature* **2013**, *499*, 419.
[19] H.-M. Li, D. Lee, D. Qu, X. Liu, J. Ryu, A. Seabaugh, W. J. Yoo, *Nat. Commun.* **2015**, *6*.
[20] K. S. Novoselov, A. K. Geim, S. V. Morozov, D. Jiang, Y. Zhang, S. V. Dubonos, I. V. Grigorieva, A. A. Firsov, *Science* **2004**, *306*, 666.
[21] J. N. Coleman, M. Lotya, A. O'Neill, S. D. Bergin, P. J. King, U. Khan, K. Young, A. Gaucher, S. De, R. J. Smith, I. V. Shvets, S. K. Arora, G. Stanton, H. Y. Kim, K. Lee, G. T. Kim, G. S. Duesberg, T. Hallam, J. J. Boland, J. J. Wang, J. F. Donegan, J. C. Grunlan, G. Moriarty, A. Shmeliov, R. J. Nicholls, J. M. Perkins, E. M. Grieveson, K. Theuwissen, D. W. McComb, P. D. Nellist, et al., *Science* **2011**, *331*, 568.
[22] J. Yu, A. A. Suleiman, Z. Zheng, X. Zhou, T. Zhai, *Adv. Funct. Mater.* **2020**, 30.
[23] J. Yu, G. Gao, W. Han, C. Wei, Y. Wang, T. Lin, T. Zhang, Z. Zheng, D. K. Ki, H. Zhang, M. H. Ng, H. Liu, S. Wang, H. Wang, F. C. C. Ling, *Adv. Electron. Mater.* **2022**, *8*.
[24] Q. Ji, Y. Zhang, Y. Zhang, Z. Liu, *Chem. Soc. Rev.* **2015**, *44*, 2587.
[25] Y. Shi, H. Li, L. J. Li, *Chem. Soc. Rev.* **2015**, *44*, 2744.
[26] K. Wang, D. Huang, X. Li, K. Feng, M. Shao, J. Yi, W. He, L. Qian, *Electron.* **2023**, *1*, e4.
[27] F. Wang, K. Pei, Y. Li, H. Li, T. Zhai, *Adv. Mater.* **2021**, *33*, 2005303.
[28] X. Xu, T. Guo, H. Kim, M. K. Hota, R. S. Alsaadi, M. Lanza, X. Zhang, H. N. Alshareef, *Adv. Mater.* **2022**, *34*, 2108258.
[29] Z. Yang, J. Hao, *J. Mater. Chem. C.* **2016**, *4*, 8859.
[30] S. V. Mandyam, H. M. Kim, M. Drndic, *JPhys. Mater.* **2020**, *3*.
[31] J. Yu, X. Hu, H. Li, X. Zhou, T. Zhai, *J. Mater. Chem. C* **2018**, *6*, 4627.
[32] Z. Wang, H. M. Huang, X. Guo, *Adv. Electron. Mater.* **2021**, *7*.
[33] Z. Wang, R. Yang, H. M. Huang, H. K. He, J. Shaibo, X. Guo, *Adv. Electron. Mater.* **2020**, *6*.
[34] C. H. Naylor, W. M. Parkin, Z. Gao, J. Berry, S. Zhou, Q. Zhang, J. B. McClimon, L. Z. Tan, C. E. Kehayias, M. Q. Zhao, R. S. Gona, R. W. Carpick, A. M. Rappe, D. J. Srolovitz, M. Drndic, A. T. C. Johnson, *ACS. Nano.* **2017**, *11*, 8619.
[35] H. Ye, J. Zhou, D. Er, C. C. Price, Z. Yu, Y. Liu, J. Lowengrub, J. Lou, Z. Liu, V. B. Shenoy, *ACS. Nano.* **2017**, *11*, 12780.
[36] N. Zhou, L. Gan, R. Yang, F. Wang, L. Li, Y. Chen, D. Li, T. Zhai, *ACS Nano* **2019**, *13*, 6297.
[37] M. Jung, S. Ji, G. Kim, S. Seok, *Chem. Soc. Rev.* **2019**, *48*, 2011.
[38] M. Qian, Y. S. Zhou, Y. Gao, J. B. Park, T. Feng, S. M. Huang, Z. Sun, L. Jiang, Y. F. Lu, *Appl. Phys. Lett.* **2011**, 98.
[39] I. Kumar, A. Khare, *Appl. Surf. Sci.* **2014**, *317*, 1004.
[40] Y. Bleu, F. Bourquard, A. S. Loir, V. Barnier, F. Garrelie, C. Donnet, *J. Raman Spectrosc.* **2019**, *50*, 1630.
[41] M. A. Shazni Mohammad Haniff, N. H. Zainal Ariffin, P. C. Ooi, M. F. Mohd Razip Wee, M. A. Mohamed, A. A. Hamzah, M. I. Syono, A. M. Hashim, *ACS Omega* **2021**, *6*, 12143.
[42] M. P. Lavin-Lopez, J. L. Valverde, S. Ordoñez-Lozoya, A. Paton-Carrero, A. Romero, *Mater. Chem. Phys.* **2019**, *222*, 173.
[43] Y. Bleu, V. Barnier, F. Christien, F. Bourquard, A. S. Loir, F. Garrelie, C. Donnet, *Carbon* **2019**, *155*, 410.
[44] G. K. Hemani, W. G. Vandenberghe, B. Brennan, Y. J. Chabal, A. V. Walker, R. M. Wallace, M. Quevedo-Lopez, M. V. Fischetti, *Appl. Phys. Lett.* **2013**, 103.
[45] P. Kumar, I. Lahiri, A. Mitra, *Results Phys.* **2019**, *14*.
[46] K. Wang, G. Tai, K. H. Wong, S. P. Lau, W. Guo, *AIP Adv.* **2011**, *1*.
[47] Y. Bleu, F. Bourquard, J.-Y. Michalon, Y. Lefkir, S. Reynaud, A.-S. Loir, V. Barnier, F. Garrelie, C. Donnet, *Appl. Surf. Sci.* **2021**, 555.
[48] M. M. Juvaid, S. Sarkar, P. K. Gogoi, S. Ghosh, M. Annamalai, Y. C. Lin, S. Prakash, S. Goswami, C. Li, S. Hooda, H. Jani, M. B. H.

Breese, A. Rusydi, S. J. Pennycook, K. Suenaga, M. S. R. Rao, T. Venkatesan, *ACS Nano.* **2020**, *14*, 3290.
[49] Y. Bleu, F. Bourquard, V. Barnier, Y. Lefkir, S. Reynaud, A. S. Loir, F. Garrelie, C. Donnet, *Appl. Surf. Sci.* **2020**, 513.
[50] Y. Bleu, F. Bourquard, T. Tite, A. S. Loir, C. Maddi, C. Donnet, F. Garrelie, *Front. Chem.* **2018**, *6*, 572.
[51] J. Wang, L. Fan, X. Wang, T. Xiao, L. Peng, X. Wang, J. Yu, L. Cao, Z. Xiong, Y. Fu, C. Wang, Q. Shen, W. Wu, *Appl. Surf. Sci.* **2019**, *494*, 651.
[52] M. M. Juvaid, D. Kumar, M. S. Ramachandra Rao, *Mater. Res. Bull.* **2020**, 126.
[53] V. Apicella, T. A. Fasasi, S. Wang, S. Lei, A. Ruotolo, *Adv. Electron. Mater.* **2019**, *5*.
[54] S. Goswami, M. Chakraborty, D. De, *IOP Conf. Ser. Mater. Sci. Eng.* **2022**, 1225.
[55] S. Gupta, P. Joshi, J. Narayan, *Carbon* **2020**, *170*, 327.
[56] G. Cassabois, P. Valvin, B. Gil, *Nat. Photonics* **2016**, *10*, 262.
[57] Q. Cai, D. Scullion, W. Gan, A. Falin, P. Cizek, S. Liu, J. H. Edgar, R. Liu, B. C. C. Cowie, E. J. G. Santos, L. H. Li, *Phys. Rev. Lett.* **2020**, *125*, 085902.
[58] Z. Cui, Y. He, H. Tian, A. Khanaki, L. Xu, W. Shi, J. Liu, *ACS Appl. Electron. Mater.* **2020**, *2*, 747.
[59] S. Hong, C. S. Lee, M. H. Lee, Y. Lee, K. Y. Ma, G. Kim, S. I. Yoon, K. Ihm, K. J. Kim, T. J. Shin, S. W. Kim, E. C. Jeon, H. Jeon, J. Y. Kim, H. I. Lee, Z. Lee, A. Antidormi, S. Roche, M. Chhowalla, H. J. Shin, H. S. Shin, *Nature* **2020**, *582*, 511.
[60] Y. Uchida, S. Nakandakari, K. Kawahara, S. Yamasaki, M. Mitsuhara, H. Ago, *ACS Nano* **2018**, *12*, 6236.
[61] D. Liu, X. Chen, Y. Yan, Z. Zhang, Z. Jin, K. Yi, C. Zhang, Y. Zheng, Y. Wang, J. Yang, X. Xu, J. Chen, Y. Lu, D. Wei, A. T. S. Wee, D. Wei, *Nat. Commun.* **2019**, *10*, 1188.
[62] J. H. Lee, D. H. Shin, H. Yang, N. B. Jeong, D. H. Park, K. Watanabe, T. Taniguchi, E. Kim, S. W. Lee, S. H. Jhang, B. H. Park, Y. Kuk, H. J. Chung, *Nat. Commun.* **2021**, *12*, 1000.
[63] K. Lee, J. Choi, B. Kaczer, A. Grill, J. W. Lee, S. Van Beek, E. Bury, J. Diaz-Fortuny, A. Chasin, J. Lee, J. Chun, D. H. Shin, J. Na, H. Cho, S. W. Lee, G. T. Kim, *Adv. Funct. Mater.* **2021**, 31.
[64] S. Pace, L. Martini, D. Convertino, D. H. Keum, S. Forti, S. Pezzini, F. Fabbri, V. Miseikis, C. Coletti, *ACS Nano* **2021**, *15*, 4213.
[65] S. M. Kim, A. Hsu, M. H. Park, S. H. Chae, S. J. Yun, J. S. Lee, D. H. Cho, W. Fang, C. Lee, T. Palacios, M. Dresselhaus, K. K. Kim, Y. H. Lee, J. Kong, *Nat. Commun.* **2015**, *6*, 8662.
[66] G. Lu, T. Wu, Q. Yuan, H. Wang, H. Wang, F. Ding, X. Xie, M. Jiang, *Nat. Commun.* **2015**, *6*, 6160.
[67] H. Tian, A. Khanaki, P. Das, R. Zheng, Z. Cui, Y. He, W. Shi, Z. Xu, R. Lake, J. Liu, *Nano Lett.* **2018**, *18*, 3352.
[68] T. A. Chen, C. P. Chuu, C. C. Tseng, C. K. Wen, H. P. Wong, S. Pan, R. Li, T. A. Chao, W. C. Chueh, Y. Zhang, Q. Fu, B. I. Yakobson, W. H. Chang, L. J. Li, *Nature* **2020**, *579*, 219.
[69] N. R. Glavin, C. Muratore, M. L. Jespersen, J. Hu, P. T. Hagerty, A. M. Hilton, A. T. Blake, C. A. Grabowski, M. F. Durstock, M. E. McConney, D. M. Hilgefort, T. S. Fisher, A. A. Voevodin, *Adv. Funct. Mater.* **2016**, *26*, 2640.
[70] G. Wang, J. Chen, J. Meng, Z. Yin, J. Jiang, Y. Tian, J. Li, J. Wu, P. Jin, X. Zhang, *Fundam. Res.* **2021**, *1*, 677.
[71] A. Biswas, Q. Ruan, F. Lee, C. Li, S. A. Iyengar, A. B. Puthirath, X. Zhang, H. Kannan, T. Gray, A. G. Birdwell, M. R. Neupane, P. B. Shah, D. A. Ruzmetov, T. G. Ivanov, R. Vajtai, M. Tripathi, A. Dalton, B. I. Yakobson, P. M. Ajayan, *Appl. Mater. Today* **2023**, 30.
[72] J. Li, Y. Li, J. Yin, X. Ren, X. Liu, C. Jin, W. Guo, *Small* **2016**, *12*, 3645.
[73] L. Wang, X. Xu, L. Zhang, R. Qiao, M. Wu, Z. Wang, S. Zhang, J. Liang, Z. Zhang, Z. Zhang, W. Chen, X. Xie, J. Zong, Y. Shan, Y. Guo, M. Willinger, H. Wu, Q. Li, W. Wang, P. Gao, S. Wu, Y. Zhang, Y. Jiang, D. Yu, E. Wang, X. Bai, Z. J. Wang, F. Ding, K. Liu, *Nature* **2019**, *570*, 91.
[74] S. Wang, A. E. Dearle, M. Maruyama, Y. Ogawa, S. Okada, H. Hibino, Y. Taniyasu, *Adv. Mater.* **2019**, *31*, 1900880.
[75] S. Roy, X. Zhang, A. B. Puthirath, A. Meiyazhagan, S. Bhattacharyya, M. M. Rahman, G. Babu, S. Susarla, S. K. Saju, M. K. Tran, L. M. Sassi, M. Saadi, J. Lai, O. Sahin, S. M. Sajadi, B. Dharmarajan, D. Salpekar, N. Chakingal, A. Baburaj, X. Shuai, A. Adumbumkulath, K. A. Miller, J. M. Gayle, A. Ajnsztajn, T. Prasankumar, V. V. J. Harikrishnan, V. Ojha, H. Kannan, A. Z. Khater, Z. Zhu, et al., *Adv. Mater.* **2021**, *33*, 2101589.
[76] A. Biswas, R. Maiti, F. Lee, C. Y. Chen, T. Li, A. B. Puthirath, S. A. Iyengar, C. Li, X. Zhang, H. Kannan, T. Gray, M. Saadi, J. Elkins, A. G. Birdwell, M. R. Neupane, P. B. Shah, D. A. Ruzmetov, T. G. Ivanov, R. Vajtai, Y. Zhao, A. L. Gaeta, M. Tripathi, A. Dalton, P. M. Ajayan, *Nanoscale Horiz.* **2023**, *8*, 641.
[77] H. Liu, A. T. Neal, Z. Zhu, Z. Luo, X. Xu, D. Tomanek, P. D. Ye, *ACS Nano.* **2014**, *8*, 4033.
[78] L. Li, Y. Yu, G. J. Ye, Q. Ge, X. Ou, H. Wu, D. Feng, X. H. Chen, Y. Zhang, *Nat. Nanotechnol.* **2014**, *9*, 372.
[79] G. Long, D. Maryenko, J. Shen, S. Xu, J. Hou, Z. Wu, W. K. Wong, T. Han, J. Lin, Y. Cai, R. Lortz, N. Wang, *Nano Lett.* **2016**, *16*, 7768.
[80] D. Hanlon, C. Backes, E. Doherty, C. S. Cucinotta, N. C. Berner, C. Boland, K. Lee, A. Harvey, P. Lynch, Z. Gholamvand, S. Zhang, K. Wang, G. Moynihan, A. Pokle, Q. M. Ramasse, N. McEvoy, W. J. Blau, J. Wang, G. Abellan, F. Hauke, A. Hirsch, S. Sanvito, D. D. O'Regan, G. S. Duesberg, V. Nicolosi, J. N. Coleman, *Nat. Commun.* **2015**, *6*, 8563.
[81] L. Li, J. Kim, C. Jin, G. J. Ye, D. Y. Qiu, F. H. da Jornada, Z. Shi, L. Chen, Z. Zhang, F. Yang, K. Watanabe, T. Taniguchi, W. Ren, S. G. Louie, X. H. Chen, Y. Zhang, F. Wang, *Nat. Nanotechnol.* **2017**, *12*, 21.
[82] Y. Xu, X. Shi, Y. Zhang, H. Zhang, Q. Zhang, Z. Huang, X. Xu, J. Guo, H. Zhang, L. Sun, Z. Zeng, A. Pan, K. Zhang, *Nat. Commun.* **2020**, *11*, 1330.
[83] J. B. Smith, D. Hagaman, H. F. Ji, *Nanotechnology* **2016**, *27*, 215602.
[84] G. Qiu, Q. Nian, M. Motlag, S. Jin, B. Deng, Y. Deng, A. R. Charnas, P. D. Ye, G. J. Cheng, *Adv. Mater.* **2018**, 30.
[85] M. Z. Bellus, Z. Yang, P. Zereshki, J. Hao, S. P. Lau, H. Zhao, *Nanoscale Horiz.* **2019**, *4*, 236.
[86] F. Zhan, B. Zheng, X. Xiao, J. Fan, X. Wu, R. Wang, *Phys. Rev. B* **2022**, 105.
[87] N. A. N. Phan, H. Noh, J. Kim, Y. Kim, H. Kim, D. Whang, N. Aoki, K. Watanabe, T. Taniguchi, G. H. Kim, *Small* **2022**, *18*, 2105753.
[88] B. Marfoua, J. Hong, *Commun. Phys.* **2022**, *5*.
[89] H. Yang, S. O. Valenzuela, M. Chshiev, S. Couet, B. Dieny, B. Dlubak, A. Fert, K. Garello, M. Jamet, D. E. Jeong, K. Lee, T. Lee, M. B. Martin, G. S. Kar, P. Seneor, H. J. Shin, S. Roche, *Nature* **2022**, *606*, 663.
[90] C. Robert, S. Park, F. Cadiz, L. Lombez, L. Ren, H. Tornatzky, A. Rowe, D. Paget, F. Sirotti, M. Yang, D. Van Tuan, T. Taniguchi, B. Urbaszek, K. Watanabe, T. Amand, H. Dery, X. Marie, *Nat. Commun.* **2021**, *12*, 5455.
[91] S. Cha, M. Noh, J. Kim, J. Son, H. Bae, D. Lee, H. Kim, J. Lee, H. S. Shin, S. Sim, S. Yang, S. Lee, W. Shim, C. H. Lee, M. H. Jo, J. S. Kim, D. Kim, H. Choi, *Nat. Nanotechnol.* **2018**, *13*, 910.
[92] M. I. Serna, S. H. Yoo, S. Moreno, Y. Xi, J. P. Oviedo, H. Choi, H. N. Alshareef, M. J. Kim, M. Minary-Jolandan, M. A. Quevedo-Lopez, *ACS Nano* **2016**, *10*, 6054.
[93] S. Kumar, A. Sharma, Y. T. Ho, A. Pandey, M. Tomar, A. K. Kapoor, E. Y. Chang, V. Gupta, *J. Alloys Compd.* **2020**, 835.
[94] N. Perea-López, A. L. Elías, A. Berkdemir, A. Castro-Beltran, H. R. Gutiérrez, S. Feng, R. Lv, T. Hayashi, F. López-Urías, S. Ghosh, B. Muchharla, S. Talapatra, H. Terrones, M. Terrones, *Adv. Funct. Mater.* **2013**, *23*, 5511.

[95] Y. Zhang, Y. Zhang, Q. Ji, J. Ju, H. Yuan, J. Shi, T. Gao, D. Ma, M. Liu, Y. Chen, X. Song, H. Y. Hwang, Y. Cui, Z. Liu, *ACS Nano* **2013**, *7*, 8963.
[96] Z. Wang, D. K. Ki, H. Chen, H. Berger, A. H. MacDonald, A. F. Morpurgo, *Nat. Commun.* **2015**, *6*, 8339.
[97] K. M. McCreary, A. T. Hanbicki, G. G. Jernigan, J. C. Culbertson, B. T. Jonker, *Sci. Rep.* **2016**, *6*, 19159.
[98] H. Tan, Y. Fan, Y. Rong, B. Porter, C. S. Lau, Y. Zhou, Z. He, S. Wang, H. Bhaskaran, J. H. Warner, *ACS Appl. Mater. Interfaces* **2016**, *8*, 1644.
[99] K. Tian, K. Baskaran, A. Tiwari, *Thin Solid Films* **2008**, *668*, 69.
[100] F. Godel, V. Zatko, C. Carrétéro, A. Sander, M. Galbiati, A. Vecchiola, P. Brus, O. Bezencenet, B. Servet, M.-B. Martin, B. Dlubak, P. Seneor, *ACS Appl. Nano Mater.* **2020**, *3*, 7908.
[101] Z. Zheng, T. Zhang, J. Yao, Y. Zhang, J. Xu, G. Yang, *Nanotechnology* **2016**, *27*, 225501.
[102] W. Jie, Z. Yang, F. Zhang, G. Bai, C. W. Leung, J. Hao, *ACS Nano* **2017**, *11*, 6950.
[103] N. Goel, R. Kumar, M. Mishra, G. Gupta, M. Kumar, *J. Appl. Phys.* **2018**, 123.
[104] S. Sinha, S. Kumar, S. K. Arora, S. N. Jha, Y. Kumar, V. Gupta, M. Tomar, *J. Appl. Phys.* **2021**, 129.
[105] L. Valdman, V. Mazánek, P. Marvan, M. Serra, R. Arenal, Z. Sofer, *Adv. Opt. Mater.* **2021**, *9*.
[106] S. Weng, W. Zhen, Y. Li, X. Yan, H. Han, H. Huang, L. Pi, W. Zhu, H. Li, C. Zhang, *Phys. Status Solidi – Rapid Res. Lett.* **2020**, *14*.
[107] W. Yang, L. Zhang, J. Xie, X. Zhang, Q. Liu, T. Yao, S. Wei, Q. Zhang, Y. Xie, *Angew. Chem. Int. Ed. Engl.* **2016**, *55*, 6716.
[108] S. Choi, J.-W. Choi, J. C. Kim, H. Y. Jeong, J. Shin, S. Jang, S. Ham, N. D. Kim, G. Wang, *Nano Energy* **2021**, 84.
[109] Q. Ye, J. Lu, Z. Zheng, W. Huang, J. Yao, G. Yang, *Adv. Opt. Mater.* **2022**, *10*.
[110] S. Seo, I. Oh, J.-C. Park, J. Lee, Y. Jung, H. Choi, J. Ryu, S. Lee, *ACS Appl. Nano Mater.* **2021**, *4*, 12017.
[111] T. Li, T. Tu, Y. Sun, H. Fu, J. Yu, L. Xing, Z. Wang, H. Wang, R. Jia, J. Wu, C. Tan, Y. Liang, Y. Zhang, C. Zhang, Y. Dai, C. Qiu, M. Li, R. Huang, L. Jiao, K. Lai, B. Yan, P. Gao, H. Peng, *Nat. Electron.* **2020**, *3*, 473.
[112] K. Liu, B. Jin, W. Han, X. Chen, P. Gong, L. Huang, Y. Zhao, L. Li, S. Yang, X. Hu, J. Duan, L. Liu, F. Wang, F. Zhuge, T. Zhai, *Nat. Electron.* **2021**, *4*, 906.
[113] F. Xu, Z. Wu, G. Liu, F. Chen, J. Guo, H. Zhou, J. Huang, Z. Zhang, L. Fei, X. Liao, Y. Zhou, *ACS Appl. Mater. Interfaces* **2022**, *14*, 25920.
[114] J. Wu, H. Yuan, M. Meng, C. Chen, Y. Sun, Z. Chen, W. Dang, C. Tan, Y. Liu, J. Yin, Y. Zhou, S. Huang, H. Q. Xu, Y. Cui, H. Y. Hwang, Z. Liu, Y. Chen, B. Yan, H. Peng, *Nat. Nanotechnol.* **2017**, *12*, 530.
[115] J. Wu, C. Qiu, H. Fu, S. Chen, C. Zhang, Z. Dou, C. Tan, T. Tu, T. Li, Y. Zhang, Z. Zhang, L. M. Peng, P. Gao, B. Yan, H. Peng, *Nano Lett.* **2019**, *19*, 197.
[116] C. Tan, M. Tang, J. Wu, Y. Liu, T. Li, Y. Liang, B. Deng, Z. Tan, T. Tu, Y. Zhang, C. Liu, J.-H. Chen, Y. Wang, H. Peng, *Nano Lett.* **2019**, *19*, 2148.
[117] J. Wu, C. Tan, Z. Tan, Y. Liu, J. Yin, W. Dang, M. Wang, H. Peng, *Nano Lett.* **2017**, *17*, 3021.
[118] Y. Song, Z. Li, H. Li, S. Tang, G. Mu, L. Xu, W. Peng, D. Shen, Y. Chen, X. Xie, M. Jiang, *Nanotechnology* **2020**, *31*, 165704.
[119] B. Li, L. Ding, P. Gui, N. Liu, Y. Yue, Z. Chen, Z. Song, J. Wen, H. Lei, Z. Zhu, X. Wang, M. Su, L. Liao, Y. Gao, D. Zhang, G. Fang, *Adv. Mater. Interfaces.* **2019**, *6*.
[120] K. Zhou, G. Shang, H. H. Hsu, S. T. Han, V. A. L. Roy, Y. Zhou, *Adv. Mater.* **2023**, *35*, 2207774.
[121] H. Xie, Z. Li, L. Cheng, A. A. Haidry, J. Tao, Y. Xu, K. Xu, J. Z. Ou, *iScience* **2022**, *25*, 103598.
[122] P. Kumbhakar, C. Chowde Gowda, P. L. Mahapatra, M. Mukherjee, K. D. Malviya, M. Chaker, A. Chandra, B. Lahiri, P. M. Ajayan, D. Jariwala, A. Singh, C. S. Tiwary, *Mater. Today* **2021**, *45*, 142.
[123] W. Ouyang, F. Teng, J. H. He, X. Fang, *Adv. Funct. Mater.* **2019**, *29*.
[124] N. V. Nguyen, N. Nguyen, J. R. Hattrick-Simpers, O. A. Kirillov, M. L. Green, *Appl. Phys. Lett.* **2021**, 118.
[125] Y. Y. Sun, M. L. Agiorgousis, P. Zhang, S. Zhang, *Nano Lett.* **2015**, *15*, 581.
[126] S. Niu, H. Huyan, Y. Liu, M. Yeung, K. Ye, L. Blankemeier, T. Orvis, D. Sarkar, D. J. Singh, R. Kapadia, J. Ravichandran, *Adv. Mater.* **2017**, *29*.
[127] R. Jaramillo, J. Ravichandran, *APL Mater.* **2019**, *7*.
[128] T. Gupta, D. Ghoshal, A. Yoshimura, S. Basu, P. K. Chow, A. S. Lakhnot, J. Pandey, J. M. Warrender, H. Efstathiadis, A. Soni, E. Osei-Agyemang, G. Balasubramanian, S. Zhang, S. F. Shi, T. M. Lu, V. Meunier, N. Koratkar, *Adv. Funct. Mater.* **2020**, *30*.
[129] T. R. Paudel, E. Y. Tsymbal, *ACS Omega* **2020**, *5*, 12385.
[130] B. Sun, S. Niu, R. P. Hermann, J. Moon, N. Shulumba, K. Page, B. Zhao, A. S. Thind, K. Mahalingam, J. Milam-Guerrero, R. Haiges, M. Mecklenburg, B. C. Melot, Y. D. Jho, B. M. Howe, R. Mishra, A. Alatas, B. Winn, M. E. Manley, J. Ravichandran, A. J. Minnich, *Nat. Commun.* **2020**, *11*, 6039.
[131] X. Wei, H. Hui, C. Zhao, C. Deng, M. Han, Z. Yu, A. Sheng, P. Roy, A. Chen, J. Lin, D. F. Watson, Y.-Y. Sun, T. Thomay, S. Yang, Q. Jia, S. Zhang, H. Zeng, *Nano Energy* **2020**, 68.
[132] M. Surendran, H. Chen, B. Zhao, A. S. Thind, S. Singh, T. Orvis, H. Zhao, J.-K. Han, H. Htoon, M. Kawasaki, R. Mishra, J. Ravichandran, *Chem. Mater.* **2021**, *33*, 7457.
[133] Y. Nishigaki, T. Nagai, M. Nishiwaki, T. Aizawa, M. Kozawa, K. Hanzawa, Y. Kato, H. Sai, H. Hiramatsu, H. Hosono, H. Fujiwara, *Solar RRL* **2020**, *4*.
[134] J. A. Marquez, M. Rusu, H. Hempel, I. Y. Ahmet, M. Kolbach, I. Simsek, L. Choubrac, G. Gurieva, R. Gunder, S. Schorr, T. Unold, *J. Phys. Chem. Lett.* **2021**, *12*, 2148.
[135] H. Fan, Z. Tan, H. Liu, L. Zhang, F. Zhang, W. Du, Z. Fan, X. Gao, F. Pan, D. Yu, Y. Zhao, *ACS Appl. Mater. Interfaces* **2022**, *14*, 17987.
[136] C. Ko, Y. Lee, Y. Chen, J. Suh, D. Fu, A. Suslu, S. Lee, J. D. Clarkson, H. S. Choe, S. Tongay, R. Ramesh, J. Wu, *Adv. Mater.* **2016**, *28*, 2923.
[137] Z. Fan, H. Fan, L. Yang, P. Li, Z. Lu, G. Tian, Z. Huang, Z. Li, J. Yao, Q. Luo, C. Chen, D. Chen, Z. Yan, M. Zeng, X. Lu, X. Gao, J.-M. Liu, *J. Mater. Chem. C* **2017**, *5*, 7317.
[138] M. Si, C. J. Su, C. Jiang, N. J. Conrad, H. Zhou, K. D. Maize, G. Qiu, C. T. Wu, A. Shakouri, M. A. Alam, P. D. Ye, *Nat. Nanotechnol.* **2018**, *13*, 24.
[139] Z. Yang, Z. Wu, Y. Lyu, J. Hao, *InfoMat* **2019**, *1*, 98.
[140] R. Wang, L. Li, L. Li, C. Zhu, Z. Li, L. Cheng, S. Feng, G. Zhang, Y. Zang, J. Hu, Y. Xu, *Mater. Lett.* **2022**, 308.
[141] S. Leontsev, P. J. Shah, H. S. Kum, J. L. McChesney, F. M. Rodolakis, M. van Veenendaal, M. Velez, R. Rao, D. Haskel, J. Kim, A. N. Reed, M. R. Page, *J. Magn. Magn. Mater.* **2022**, 556.
[142] R. Attri, M. B. Sreedhara, C. N. R. Rao, *ACS Appl. Electron. Mater.* **2019**, *1*, 569.
[143] M. Cesaria, A. Lorusso, A. P. Caricato, P. Finocchiaro, S. Amaducci, M. Martino, M. R. Aziz, L. Calcagnile, A. Perrone, G. Quarta, *Appl. Phys. A* **2020**, 126.
[144] A. A. Muhanad, M. F. Mohammed Sabri, W. R. Abed, *ARO* **2021**, *9*, 46.
[145] I. Sebarchievici, B.-O. Taranu, S. F. Rus, E. Fagadar-Cosma, *J. Electroanal. Chem.* **2020**, *865*, 114127.
[146] D. D. Baciu, R. Bîrjega, V. Mărăscu, R. Zăvoianu, A. Matei, A. Vlad, A. Cojocaru, T. Visan, *Surf. Interfaces* **2021**, *24*.
[147] M. F. H. A. El-Kader, M. K. Ahmed, M. T. Elabbasy, M. Afifi, A. A. Menazea, *Surf. Coat. Technol.* **2021**, 409.

[148] Z. Jin, H. Zhou, X. Zhang, K. Cao, R. Chen, *ACS Mater. Lett.* **2023**, *5*, 803.
[149] K. Gu, Y. Guan, B. K. Hazra, H. Deniz, A. Migliorini, W. Zhang, S. S. P. Parkin, *Nat. Nanotechnol.* **2022**, *17*, 1065.
[150] L. Ghosh, M. Alam, M. Singh, S. Dixit, S. V. Kumar, A. Verma, P. Shahi, Y. Uwatoko, S. Saha, A. Tiwari, A. Tripathi, S. Chatterjee, *Nanoscale* **2022**, *14*, 10889.
[151] C. H. Suen, L. Zhang, K. Yang, M. Q. He, Y. S. Chai, K. Zhou, H. Wang, X. Y. Zhou, J.-Y. Dai, *J. Materiomics* **2022**, *8*, 570.
[152] J.-C. Park, S. Kim, H. Choi, Y. Jung, I. Oh, J. B. Hwang, S. Lee, *Cryst. Growth Des.* **2023**, *23*, 2092.
[153] M. A. Fakhri, M. J. AbdulRazzaq, H. D. Jabbar, E. T. Salim, F. H. Alsultany, U. Hashim, *Opt. Mater.* **2023**, 137.
[154] V. Zatko, S. M. Dubois, F. Godel, C. Carretero, A. Sander, S. Collin, M. Galbiati, J. Peiro, F. Panciera, G. Patriarche, P. Brus, B. Servet, J. C. Charlier, M. B. Martin, B. Dlubak, P. Seneor, *ACS Nano* **2021**, *15*, 7279.
[155] R. Salazar, S. Varotto, C. Vergnaud, V. Garcia, S. Fusil, J. Chaste, T. Maroutian, A. Marty, F. Bonell, D. Pierucci, A. Ouerghi, F. Bertran, P. Le Fevre, M. Jamet, M. Bibes, J. Rault, *Nano Lett.* **2022**, *22*, 9260.
[156] P. D'Agosta, F. Tumino, V. Russo, A. Li Bassi, C. S. Casari, *Nanoscale* **2023**, *15*, 7493.
[157] Z. Sha, R. Jia, S. Ma, F. Xia, J. Tian, L. Yu, L. Dong, *J. Alloys Compd.* **2022**, 906.
[158] F. Tumino, A. Rabia, A. L. Bassi, S. Tosoni, C. S. Casari, *J. Phys. Chem. C* **2022**, *126*, 1132.

Jing Yu received her B.S. degree in functional materials from Lanzhou University (LZU) in 2017, and then received her Master degree in Materials from the School of Materials Science and Engineering, Huazhong University of Science and Technology (HUST) in 2020. She is now a Ph.D. candidate in the Department of Physics, Faculty of Science, the University of Hong Kong (HKU). Her research is focused on synthesis of thin films via PLD method.

Abdulsalam Aji Suleiman received his Ph.D. degree in materials science in 2021 from the Huazhong University of Science and Technology, China. He is currently a postdoctoral fellow at the National Nanotechnology Research Center (UNAM), Bilkent University, Turkey. His current work focuses on the synthesis and characterization of 2D materials for electrical and optoelectronic device applications.

Naihua Miao is a Professor in the School of Materials Science and Engineering at Beihang University, Beijing, China. He received his B. Sc. (2008) and M. Sc. (2011) in materials science from Xiamen University (China), and a Ph.D. (2015) in condensed matter physics from the University of Liege (Belgium). His research interest includes the development of theoretical methodologies based on quantum mechanics and artificial intelligence, and their applications in the discovery of new advanced (bulk and 2D) materials.

Francis Chi-Chung Ling is an Associate Professor at The University of Hong Kong. He obtained a Fellow of the Institute of Physics in 2006. He received his B.Sc., M.Ph., and Ph.D. from the University of Hong Kong in 1990, 1993, and 1996, respectively. His current research focuses on developing new functionality of wide band gap semiconductors, tailoring materials properties, and improving device performance via defect engineering. He has a strong tie-up with the SiC industry in the research and development of power devices.